

## RESEARCH ARTICLE

10.1002/2014JC010693

## Key Points:

- Strong interaction between warm and cold ambient waters formed an anticyclone
- Multilayer structure and remnant layer formed via repeated interactions
- Changes in propagation pattern linked to interior structure of the anticyclone

## Correspondence to:

H. Kaneko,  
kaneko@aori.u-tokyo.ac.jp

## Citation:

Kaneko, H., S. Itoh, S. Kouketsu, T. Okunishi, S. Hosoda, and T. Suga (2015), Evolution and modulation of a poleward-propagating anticyclonic eddy along the Japan and Kuril-Kamchatka trenches, *J. Geophys. Res. Oceans*, 120, doi:10.1002/2014JC010693.

Received 2 JAN 2015

Accepted 27 MAY 2015

Accepted article online 29 MAY 2015

## Evolution and modulation of a poleward-propagating anticyclonic eddy along the Japan and Kuril-Kamchatka trenches

Hitoshi Kaneko<sup>1</sup>, Sachihiko Itoh<sup>1</sup>, Shinya Kouketsu<sup>2</sup>, Takeshi Okunishi<sup>3</sup>, Shigeki Hosoda<sup>2</sup>, and Toshio Suga<sup>2,4</sup>

<sup>1</sup>Atmosphere and Ocean Research Institute, University of Tokyo, Chiba, Japan, <sup>2</sup>Research Institute for Global Change, Japan Agency for Marine-Earth Science and Technology, Yokosuka, Japan, <sup>3</sup>National Research Institute of Fisheries Science, Fisheries Research Agency, Yokohama, Japan, <sup>4</sup>Department of Geophysics, Graduate School of Science, Tohoku University, Sendai, Japan

**Abstract** To investigate the relationships between the movement of an eddy and its interior structure and water properties, four profiling floats were deployed in an anticyclonic eddy in the western North Pacific in 2013 (April–October). Daily float profiles showed rapid changes in temperature and salinity corresponding to strong interactions between eddies north of the subtropical Kuroshio Extension. After the first interaction with a warm-core eddy in April, the isolation of the winter mixed layer from the surface was observed, forming a subsurface remnant layer. Another interaction with a cold fresh eddy at middepths in May resulted in the formation of a multilayer structure. The eddy then moved poleward along the Japan and Kuril-Kamchatka trenches, indicating changes in its propagation pattern coupled to its interior structure. The eddy then moved northward (June–July), stalled (July–August), and moved eastward (August–October). In addition to a general declining trend, the properties of the warm saline core changed over a short time period, coinciding with changes in propagation. A density anomaly at middepths of the eddy changed location during the stalled period; however, denser waters were continuously observed in the southeast part of the eddy during its northward and eastward movement. This unidirectional density anomaly pattern was consistent with the structure of the poleward-propagating eddy, which interacted with the western topographic boundary. Meridional exchanges of heat and material were potentially elevated by the eddy's advection and movement, as well as by water modifications in the eddy associated with exchanges along its perimeter.

### 1. Introduction

Mesoscale anticyclonic eddies (ACEs) generally have longer lifetimes (several months to years) than cyclonic eddies and frequently propagate away from the regions where they formed. Thus, ACEs play important roles in the transport and exchange of heat, materials, and biota [e.g., Olson, 1991, 2001; Roemmich and Gilson, 2001; Qiu and Chen, 2005; Dong et al., 2014]. ACEs are sometimes pinched off from meanders of the western boundary currents of subtropical gyres, such as the Kuroshio Extension [Sugimoto et al., 1992; Yasuda et al., 1992] and the Gulf Stream [Elliott, 1982; Joyce et al., 1984, 1992; Olson, 1986]. These ACEs generally contain warm saline waters, and thus contribute to intergyre exchanges. Moreover, Agulhas rings shed from the Agulhas Retroflection contribute to interbasin exchange from the South Indian Ocean to the South Atlantic [Gordon, 1985; Byrne et al., 1995; Boebel et al., 2003; Richardson, 2007]. ACEs shed from the East Australian Current in the Tasman Sea [Nilsson and Cresswell, 1980; Cresswell, 1982] also contribute to transport between separated basins because they propagate along the east and south coasts of Australia and sometimes reach the Indian Ocean.

Whereas there are many propagating ACEs (generally westward) throughout the entire basin, in the northwest region of the North Pacific, warm-core rings pinched from the subtropical gyre frequently propagate northward along the Japan Trench between the Kuroshio Extension (subtropical) and Oyashio (subarctic) currents [Sugimoto et al., 1992; Yasuda et al., 1992; Isoguchi and Kawamura, 2006]. These northward-propagating ACEs sometimes cross the subtropical-subarctic gyre boundary (the subarctic front). In contrast,

around this region, the influence of subarctic waters on subtropical waters is frequently observed as the formation of a vertical salinity minimum at middepths, which spreads to the subtropical gyre as North Pacific Intermediate Water [e.g., Yasuda *et al.*, 1996].

This poleward propagation is neither similar to that of general westward-propagating Rossby waves in the open ocean under the  $\beta$  effect nor to that of topographic Rossby waves. On the basis of the statistical analysis of an eddy trajectory provided by satellite observations, Itoh and Yasuda [2010a] observed “an eddy corridor,” an area of frequent eddy propagation along the Japan Trench and Kuril-Kamchatka trenches; similarly, Itoh and Yasuda [2010a] reported ACEs with a warm core propagating northward from the subtropical gyre. Itoh and Yasuda [2010a] also suggested that the poleward heat flux caused by the movement of eddies (including cyclonic eddies as well as ACEs) is comparable to the total poleward eddy heat flux between 30°N and 40°N ( $\sim 0.1$  PW) [Jayne and Marotzke, 2002; Qiu and Chen, 2005]. Although warm-core ACEs generally occur on other western boundary currents as mentioned above, such long-lasting poleward propagation has seldom been observed in the Gulf Stream [Itoh and Sugimoto, 2001] or other regions in the North Pacific [Cheng *et al.*, 2014].

In addition to their importance for horizontal heat transport in the oceans, poleward ACEs can function as efficient heat radiators from the ocean to atmosphere because wintertime atmospheric cooling can force warm-core ACEs to drastically lose heat. A 5–6°C decrease in the typical temperature of the Kuroshio Extension (14–15°C) in the upper warm core of ACEs was observed during the first winter after their formation [Tomosada, 1986; Yasuda *et al.*, 1992]. Sugimoto and Hanawa [2011] demonstrated that the increase in the number of ACEs detached from the Kuroshio Extension under the convoluted state of the gyre compared with the straight path state could contribute to positive sea surface temperature (SST) anomalies in the transition region between the Kuroshio Extension and the Oyashio Current, which would lead to a large amount of heat release. This heat release could lead to the development of a deep mixed layer during winter, and thus the formation of a pycnostad (low-potential vorticity) within each ACE in the subsequent season [Kouketsu *et al.*, 2012].

Poleward-propagating ACEs also have a strong impact on biota. Warm water streams extending from the Kuroshio Extension into the periphery of ACEs are important pathways for northward migration of pelagic fish, such as skipjack tuna (*Katsuwonus pelamis*), chub mackerel (*Scomber japonicus*), Japanese common squid (*Todarodes pacificus*), and Pacific saury (*Cololabis saira*), and consequently become good fishing areas for these species [Kawai and Sasaki, 1962; Sugimoto and Tameishi, 1992]. The occurrence of nearshore, warm-core rings off Hokkaido, the western boundary region of the subarctic gyre, could result in a concentrated migration of sauries east of the rings, and thus, fishery grounds farther away from Hokkaido [Yasuda and Watanabe, 1994]. The transition region between the Kuroshio Extension and the Oyashio Current is important to both adult fish and their larvae, because the region serves as a nursery ground for larvae that spawned in the subtropical gyre during the spring [Ito *et al.*, 2004; Watanabe, 2007; Okunishi *et al.*, 2012]. The environment of this area critically affects larvae survival and abundance through the recruitment of these fish [e.g., Nishikawa *et al.*, 2011]. Moreover, vertical nutrient transport near fronts along ACE peripheries is important for sustaining phytoplankton production through enhanced transport around the Kuroshio Extension [Kaneko *et al.*, 2013]. Therefore, the evolution and fate of ACEs through interactions between currents and ambient waters have a great impact on commercial fishery resources, in addition to the transport of heat, material, and potential vorticity in the western North Pacific.

Interactions between warm water from the Kuroshio Extension and cold water from the subarctic are one of the main factors controlling ACE evolution. Such interactions sometimes result in the subsequent drastic intensification of an ACE [Yasuda *et al.*, 1992, 2000; Itoh *et al.*, 2011a, 2014a]. On the basis of repeated shipboard observations and satellite images, Yasuda *et al.* [1992] reported an increase in the size and isolation of a warm-core ACE (named 86B) from the Kuroshio Extension after its contact with a warm-tongue structure from the current. In addition, Yasuda *et al.* [2000] demonstrated the intensification of an ACE located near Bussol' Strait due to its interaction with low-potential vorticity water flowing out from the Sea of Okhotsk. As low-potential vorticity water formed by intense tidal mixing around the Kuril Islands [e.g., Itoh *et al.*, 2010, 2011b, 2014b; Yagi and Yasuda, 2012] flows along the Japan and Kuril-Kamchatka trenches, the ACEs along the trenches could be affected by this water mass.

Using two profiling floats from 2003 to 2004, Itoh *et al.* [2011a] revealed the entrainment of cold fresh water from the Sea of Okhotsk into the northeastward ACE and the subsequent change in core-water temperature

(warm to cold), which resulted in the detrainment of the floats before the ACE completely decayed. Moreover, by employing three profiling floats that were gradually deployed from 2009 to 2010, *Itoh et al.* [2014a] reported that a thick cold-core ACE from the Sea of Okhotsk combined with a warm-core ACE, coinciding with the intrusion of cold water beneath the warm core. The cold-water intrusion into the middepths could have led to the cooling and shrinking of the warm-core ring above the cold water [*Itoh et al.*, 2014a].

In addition to intrusions, the interior structures of ACEs can also influence their fate via their poleward movement. For example, based on transects of ACEs crossing the Japan and Kuril-Kamchatka trenches, *Itoh and Yasuda* [2010b] pointed out that the centers of the ACEs tilted offshore with increasing depth. Such tilting could lead to net poleward heat transport because of the positive correlation between temperature and latitudinal velocity in the case of warm-core rings; the centers of the warm cores of eddies mainly correspond to northward velocities, whereas the relatively cold peripheries correspond to mostly southward velocities [*Roemmich and Gilson*, 2001]. This tilting of the axis also suggested interactions between ACEs and topography, which were consistent with the results of *Itoh and Sugimoto* [2001], who emphasized the poleward movement of ACEs due to the image effect. As net heat transport enables positive temperature anomalies to move poleward, the tilting of ACEs would contribute to efficient heat transport along the Japan Trench and the Kuril-Kamchatka trench in combination with the image effect.

Previous observational studies on ACEs as mentioned above have demonstrated rapid changes in physical properties, including temperature and salinity within ACEs, despite their geostrophic features [e.g., *Yasuda et al.*, 2000; *Itoh et al.*, 2011a, 2014a]. In addition, they have also reported structural characteristics, such as the alignment of warm waters above cold waters [*Itoh et al.*, 2014a] and a tilted axis [*Itoh and Yasuda*, 2010b]. However, because the time scales of such interactions are shorter than 1 month, previous shipboard observations with typical intervals of 1–2 months [e.g., *Yasuda et al.*, 1992] only roughly resolved the evolution of ACEs just before and after interactions. Moreover, the temporal (5 or 10 days) and spatial (one or two floats per one ACE) resolutions of observations obtained by profiling floats were sparse relative to the phenomenon [*Itoh et al.*, 2011a, 2014a]. Thus, many questions about the changes in an ACE's movement relative to changes in its interior structures due to interactions and water-mass modifications have been left unanswered. Observations with higher temporal and spatial resolution are required to clarify how interactions and changes in properties occur, what happens within ACEs after interactions, and how the changes in the structures within ACEs are related to the movement of the eddies. Moreover, because of the lack of sufficiently long time series of observations describing the evolution of the interior structure of ACEs, there is a poor understanding of the time scales of temporal changes in the correlations of velocities and temperatures associated with the poleward movement of ACEs. Thus, our understanding of the time scale of north-south heat transport in the western North Pacific remains unclear as well.

Therefore, in the present study, the spatial structure of an ACE and its temporal development was investigated by employing four profiling floats with 1 day ascents (a higher temporal resolution than that of *Itoh et al.* [2011a, 2014a]), satellite observations, and two shipboard observations. This investigation serves as a case study to clarify the relationships between the evolution of ACE interior structures and water mass modifications due to interactions and ACE movement. The detailed investigation of the interior structure of the ACE and its evolution, focusing on poleward movement, will progress our understanding of the complicated interactions between subtropical and subarctic waters in the western North Pacific via ACE activity.

The remainder of this paper is organized as follows. The data obtained from the profiling floats, shipboard observations, and satellites are described in section 2. The structures of the observed ACE and its temporal development are demonstrated in section 3, with a focus on the marked interactions in springtime and the evolution of interior structures during poleward movement. Finally, the relationships between the interior structures and poleward movement patterns of ACE are discussed in section 4, focusing on their contributions to the eddy corridor.

## 2. Materials and Methods

We deployed an Autonomous Profiling Explorer (APEX, Teledyne Webb Research), equipped with a conductivity-temperature-depth (CTD; SBE41-CP, SeaBird Electronics) sensor. Four floats (A–D) were simultaneously deployed from the R/V *Hakuho-maru* into the target ACE, centered at 41°N and 147°E, and they first ascended on 6 April 2013 (Figure 1). The floats were configured to stay at 500 dbar, and they obtained

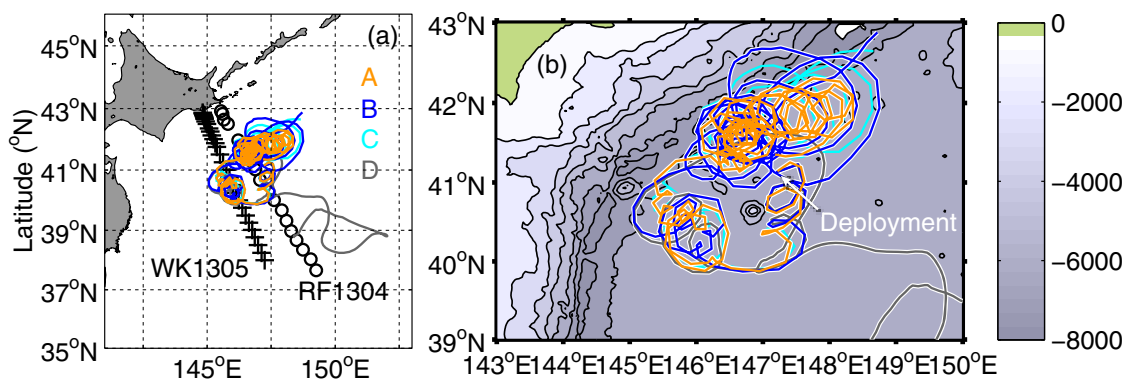


**Figure 1.** (a) Overview of study sites and float trajectories, and (b) topographical map of the study area (color and contours). The crosses (circles) in Figure 1a denote the WK1305 (RF1304) cruise stations.

profiles from 1000 dbar to the surface every day at 1300 UTC (during the local night time, 2200 Japan Standard Time). The floats A–C moved within the ACE until October 2013. In contrast, float D detrained from the ACE in late May, and thus we did not use its data collected after June for analyses together with that of the other floats. All the floats functioned until late October (Table 1). Note that the data obtained from the profiling floats had a vertical resolution of about 5, 10, and 20 dbar at depths from the surface of 200, 200–500, and 500–1000 dbar, respectively.

In addition to the profiling float data, we also used daily absolute dynamic topography (ADT) and sea surface height anomaly (SSHA) data with a resolution of  $1/4^\circ$  provided by the Segment Sol multimissions d'altimétrie, d'Orbitographie et de localisation précise/Data Unification and Altimeter Combination System (SSALTO/DUACS) and distributed by the Archiving, Validation, and Interpretation of Satellite Oceanographic Data (AVISO) project, with support from the Centre National d'Etudes Spatiales (CNES). We also used the satellite sea surface temperature (SST) maps provided by the Group for High Resolution Sea Surface Temperature (GHRSSST) as the GHRSSST multiproduct ensemble (GMPE), via The Centre ERS d'Archivage et de Traitement (CERSAT), French Research Institute for Exploitation of the Sea.

We visually detected the examined ACE after an automatic extraction of ACEs in the western North Pacific on ADT maps following the method used by *Itoh and Yasuda* [2010a]. Next, following the method of *Itoh and Yasuda* [2010b], the eddy's center was determined based on the gravitational center of relative vorticity. The eddy's area was defined by the Okubo-Weiss parameter,  $W$ . The area in  $W$  is less than the critical value of  $-2 \times 10^{-12} \text{ s}^{-2}$  for more than four grid cells [Chelton *et al.*, 2007] and  $W = 4[(\partial u/\partial x)^2 + (\partial v/\partial x)(\partial u/\partial y)]$ . A negative value of  $W$  indicates that rotation is dominant over deformation.

We analyzed CTD (SBE9plus, SeaBird Electronics) data obtained from two contemporary shipboard observations on the R/V *Wakataka-maru* (WK1305 cruise, data were obtained from 9 to 22 May) and the R/V *Rhofu-maru* (RF1304 cruise, data were obtained from 16 to 21 May) of the Tohoku National Fisheries Research Institute and Japan Meteorological Agency, respectively (Figure 1a).

We defined mixed layer depth as the depth at which the density dropped by  $0.02 \text{ kg m}^{-3}$  [e.g., *Cisewski et al.*, 2005] from the density at 5 dbar (or the shallowest available depth).

### 3. Results

#### 3.1. Propagation Pattern of ACE From April to October 2013

After the deployment of the floats near  $41^\circ\text{N}$  and  $147^\circ\text{E}$ , the ACE merged with another ACE that had pinched off from the Kuroshio Extension from mid-April to May during its southward movement (Figure 2a). Subsequently, the ACE rapidly moved northward until the end of May (Figure 2b). After this rapid northward movement, float D was

**Table 1.** Dates of Final Ascents and Number of Profiles Recorded for Each Float

Float	Final Ascent Date	Number of Profiles
A	24 Oct 2013	202
B	29 Oct 2013	207
C	24 Oct 2013	202
D	20 Oct 2013	198

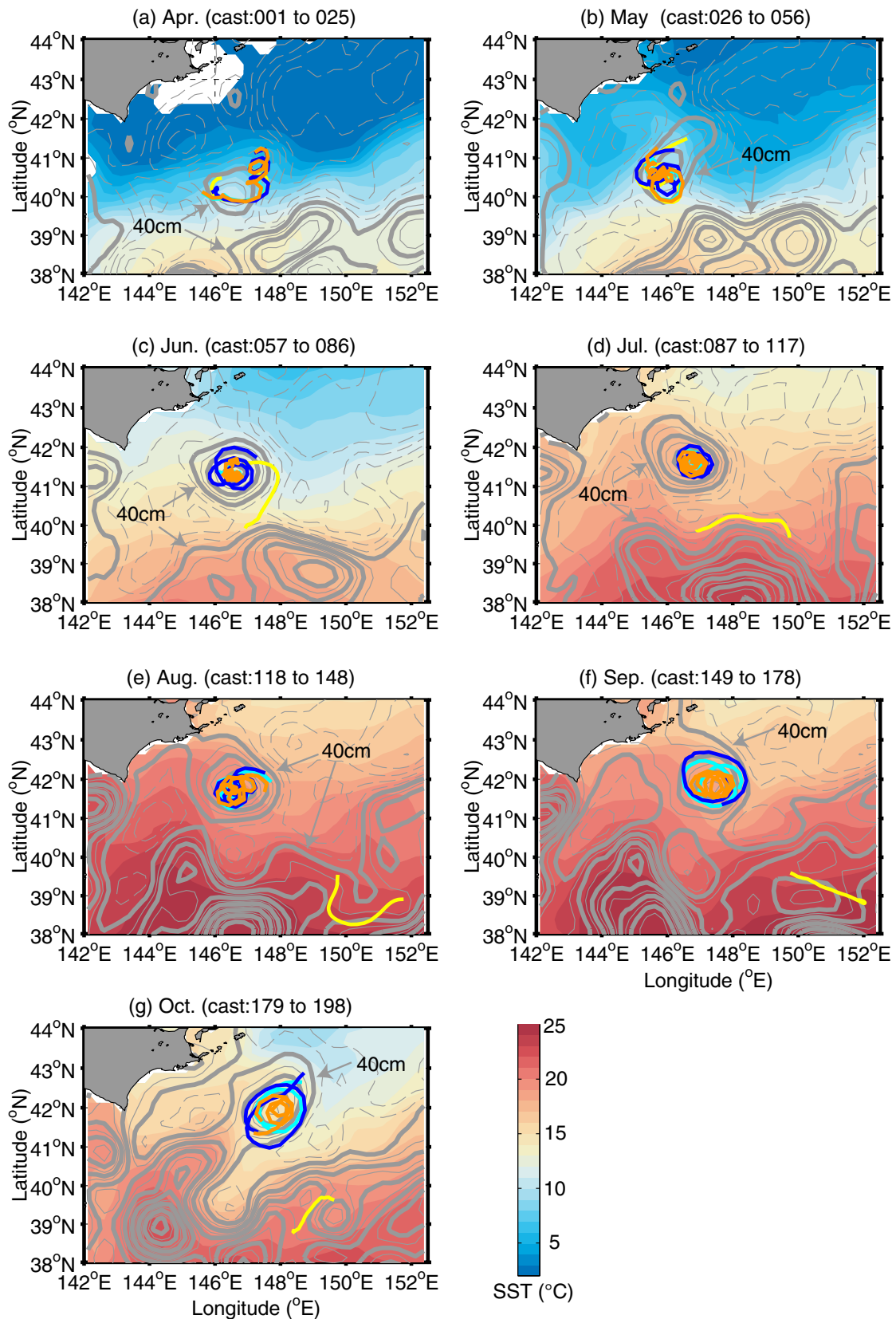


**Figure 2.** Monthly averages of sea surface temperature (SST, color shading) and absolute dynamic topography (ADT, contours) with the float trajectories during each month. The thick contours denote ADTs larger than 40 cm.

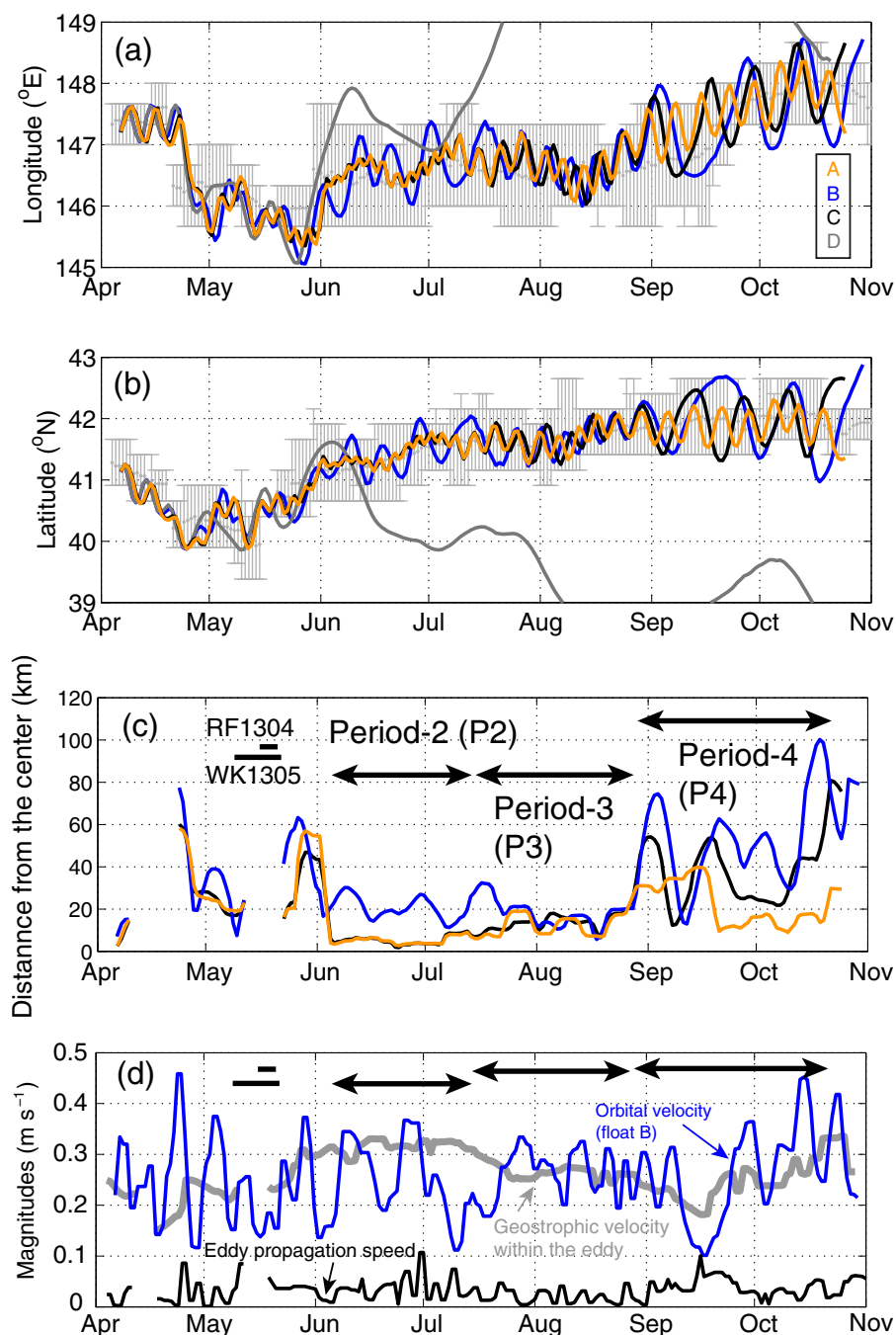


**Figure 3.** Time series of float positions. (a) Longitude and longitudinal extent (gray bars) of the core area (with a negative  $W$  value) [Itoh and Yasuda, 2010a] of the eddy as estimated from the SSH anomaly. (b) Same as Figure 3a but for latitude. (c) Distance of the floats from the center of the eddy. (d) Magnitudes of geostrophic velocity averaged within the eddy, orbital velocity estimated from the ascending positions of float B, and eddy propagation speed calculated from the center position.

detained from the ACE in early June (Figure 2c). Until this point, the trajectories of the four floats were very similar.

In June, the ACE became enlarged showing an increase in the ADT (Figure 2c). The remaining three floats (A, B, and C) rotated inside the ACE after this enlargement and were trapped in the ACE until October (Figures 2c–2g). During this period, some changes in the propagation pattern of the ACE’s and floats’ trajectories occurred about every 40–55 days (Figure 3). In the early part of the period (June), the ACE gradually

**Table 2.** Dates and Cast Numbers for Each Period<sup>a</sup>

Period	Movement Features	Date	Cast Nos.
P-1	Interaction	6 Apr 2013 to 4 Jun 2013	1–60
P-2	Northward	5 Jun 2013 to 14 Jul 2013	61–100
P-3	Stalled	15 Jul 2013 to 28 Aug 2013	101–145
P-4	Eastward	29 Aug 2013 to 22 Oct 2013	146–200

<sup>a</sup>We omitted profiles from P-4 after 200 casts.

moved northward along the Japan Trench ( $\sim 146.5^{\circ}\text{E}$ ,  $40^{\circ}\text{N}$ – $41^{\circ}\text{N}$ ; Figures 3a and 3b), and after that, the ACE was stalled off Hokkaido from July to mid-August. In late August, the ACE began to move again, to the east, and continued its northeastward propagation until October ( $146.5^{\circ}\text{E}$ – $148^{\circ}\text{E}$ ,  $\sim 42^{\circ}\text{N}$ ; Figures 3a

and 3b). From June to September, the ADT contours greater than 40 cm, which corresponded to the ACE, were almost separate from those located south of  $40^{\circ}\text{N}$ , which represented the northern edge of the Kuroshio Extension meander (Figures 2c–2f). After the end of the float observation period (29 October), the ACE turned southwestward, decreasing in radius until early December, and its center was located near  $42^{\circ}\text{N}$ ,  $147.5^{\circ}\text{E}$ ; it then showed a frequent connection to the ADT crest branched from the Kuroshio Extension (not shown).

The trajectories of the three floats A–C within the ACE from June to October also indicated changes in radii of rotation (Figure 3c). From June to mid-July, during which the ACE moved northward, floats A and C stayed near the center of the ACE, whereas float B generally rotated near the outer part. In contrast to this separation, the three floats rotated showing a similar range of radii (10–20 km) from mid-July to mid-August, during which the ACE was stalled. They were separated again from mid-August to October when the ACE moved to the east; float A was nearest the center, followed by float C, and finally by float B.

The magnitude of the geostrophic velocity averaged within the ACE showed several months variation associated with the movement of the floats (Figure 3d). The magnitude was higher from June to November ( $0.25$ – $0.3\text{ m s}^{-1}$ , except mid-September), when the floats were trapped within the ACE, than from April to May ( $0.15$ – $0.25\text{ m s}^{-1}$ ), when the floats showed drastic movement rather than rotation relative to the ACE center. The orbital velocity estimated from the ascending position of float B is consistent with the magnitude of the geostrophic velocity, especially from August to November, although the orbital velocity showed prominent shorter-term variation. In contrast, the eddy's propagating speed, as estimated from its center position, was  $0.025$ – $0.05\text{ m s}^{-1}$ , which is generally much lower than the magnitude of the geostrophic velocity.

Based on the behavior of the ACE estimated from the ADT and the trajectories of the floats as mentioned above, we divided the observed time frames into four periods for descriptive purposes (Table 2): (1) interaction (P-1; April to May), (2) northward (P-2; June to mid-July), (3) stalled (P-3; mid-July to late-August), and (4) eastward (P-4; late-August to October). We refer to the eddy-like structures that contained floats during P-1 as Pre-ACE13 (including the mergers in April and May), and to the ACE after the enlargement in early June as the isolated ACE13 because the ADT contours of  $>40\text{ cm}$  that corresponded to the ACE were generally separate from those in the Kuroshio Extension from P-2 to P-4 (Figures 2c–2f), and the three floats remained trapped during these periods.

### 3.2. Temperature and Salinity Profiles in and Around Pre-ACE13 and ACE13

The float trajectories were close together until early May, and thus the temperature and salinity time series obtained from each float showed similar features over this time. The time series indicated that a vertically homogeneous layer occurred above 300 dbar during P-1 (Figure 4); the temperature during this time was  $4.7$ – $4.9^{\circ}\text{C}$ , the salinity was  $33.65$ – $33.7\text{ psu}$ , and the density was  $26.6$ – $26.7\text{ } \sigma_{\theta}$ . The temperature and salinity in this homogeneous layer were similar to those reported by Itoh *et al.* [2011a] for an overwintered warm-core ring, suggesting that the eddy in which the floats were deployed had experienced one winter since it was detached from the Kuroshio Extension. Indeed, according to some profiling floats that were deployed into the ACE before the winter and stayed in the ACE during the winter, the occurrence of saline water ( $>34\text{ psu}$ ) was indicated at  $\sim 100\text{ dbar}$  in November 2012 (V. Faure, personal communication, 2014). Note that just after the deployment, this vertically homogeneous layer almost outcropped to the surface; however, warm and saline water appeared near the surface around 10 April, and the homogeneous layer was rapidly isolated from the surface. Thus, we defined the homogeneous layer at  $26.6$ – $26.7\text{ } \sigma_{\theta}$  after its isolation from

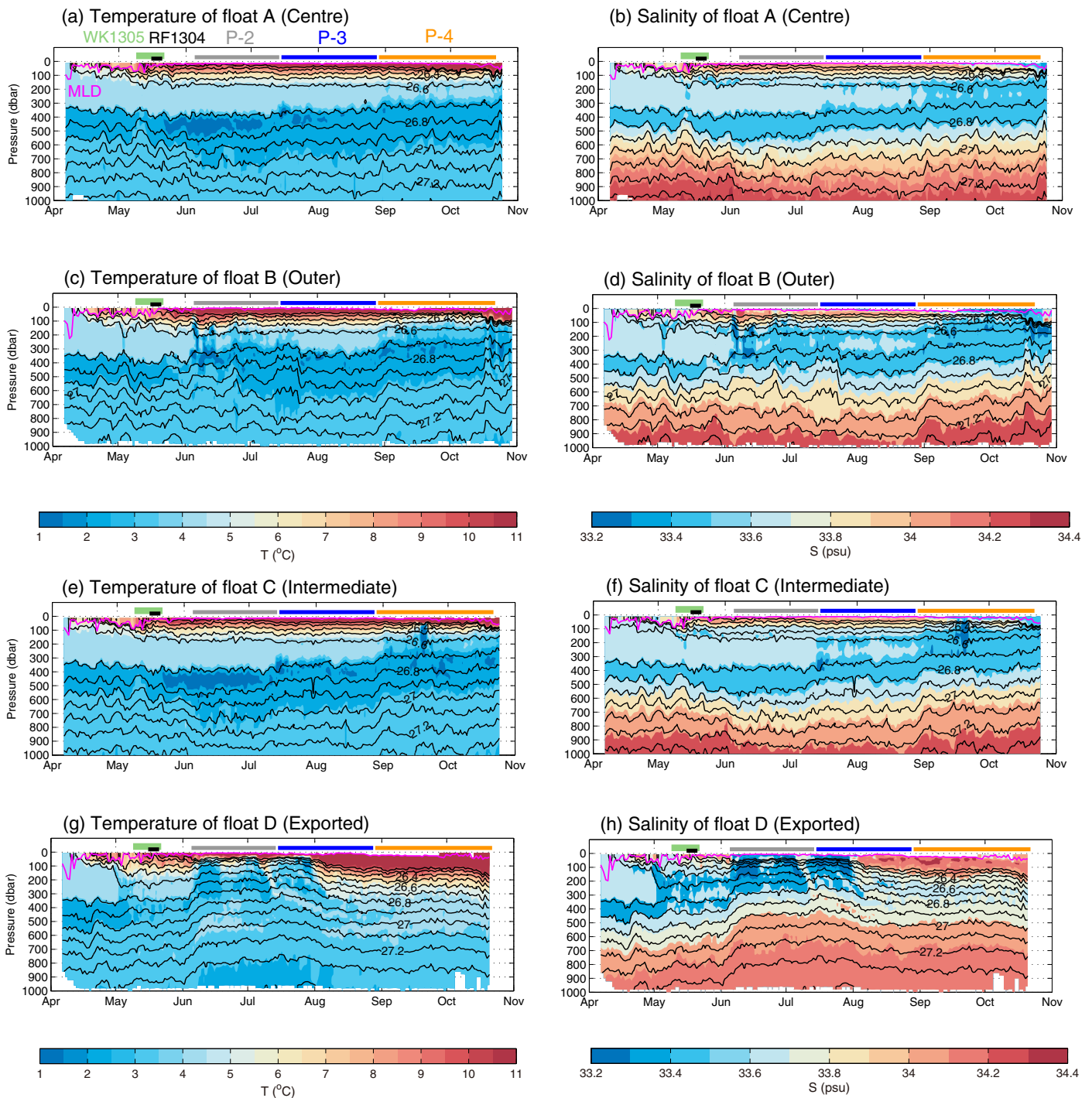


**Figure 4.** Evolution of (left column) temperature and (right column) salinity profiles as observed by (a and b) float A and (c and d) float B. The contours denote potential density. Profiles observed by (e and f) float C and (g and h) float D.

the surface as the “remnant layer” of the winter mixed layer. The remnant layer was observed at 150–300 dbar until autumn (except by float D, which escaped from ACE13); it was most prominent in the profiles from float A and decreased in thickness due to erosion by cold and fresh waters (Figures 4a and 4b).

In addition to the declining trend in the remnant layer, the profiles (except the detrained float D) showed two kinds of temporal change: midterm (~50 days) changes associated with each period defined from the

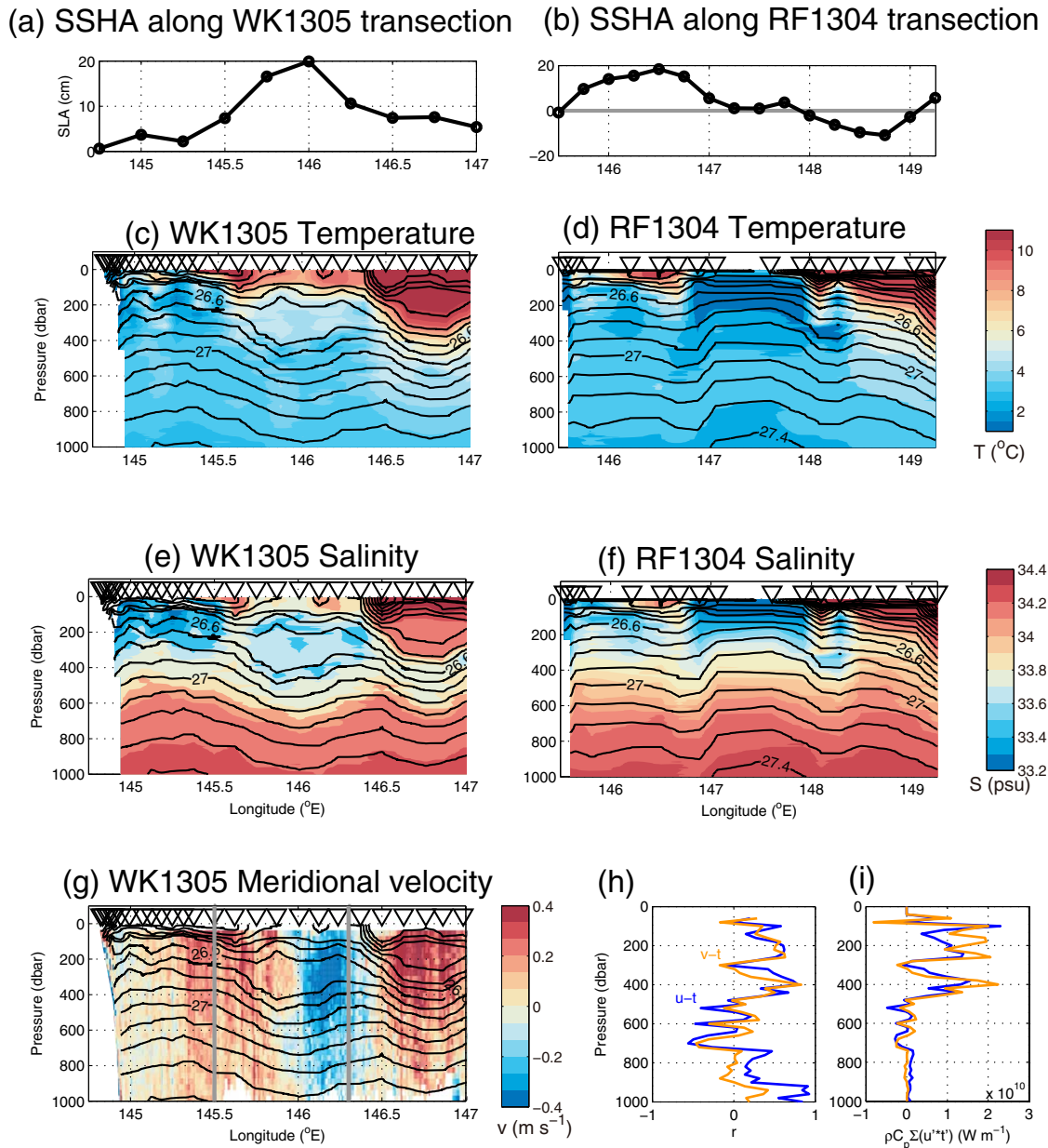


**Figure 5.** Latitudinal distributions of the sea surface height anomaly (SSHA) along (a and b) the transects, (c and d) the vertical temperature transects, (e and f) the vertical salinity transects, and (g) meridional velocity. The right (left) column is along the WK1305 (RF1304) sections. The contours denote potential density. Vertical distribution of (h) correlation coefficients between temperature and velocity, and (i) heat transport in the eddy.

trajectories of floats in section 3.1 and shorter-term variations indicated by the oscillations of the isopycnals. For example, float B showed midterm changes in the thickness of the 26.6–26.7  $\sigma_\theta$  density layer associated with each period (thick P-1, thin P-2, thick P-3, and thin P-4) (Figures 4c and 4d). As additional midterm changes, floats A and C encountered a sudden distinct cold-water layer (<2°C) beneath the remnant layer at a density of 26.7–26.8  $\sigma_\theta$  from mid-May to July (Figures 4a and 4e, respectively).

With regard to the interior of Pre-ACE13 just before the formation of ACE13, vertical sections obtained during the WK1305 (from 9 to 22 May) and RF1304 (from 16 to 21 May) cruises revealed a vertically aligned-layer structure of the ACE (Figure 5). During the shipboard observations, the floats were located around the southwestern part of Pre-ACE13 (40°N–40.5°N, ~145°E) relative to the center (Figure 2b). The WK1305 transect just crossed Pre-ACE13, which was centered at 40.5°N, 146°E, and thus an elevation in SSHA associated with Pre-ACE13 was clearly represented between 145.25°E and 146.5°E along the WK1305 transect

(Figure 5a). As Pre-ACE13 extended to the northeast during this time (Figure 2b), the edge of Pre-ACE13 was also recognized as an elevation in SSHA between 145.5°E and 147°E in the RF1304 transect, which was conducted around the same time as and east of the WK1305 transect (Figure 5b). Concerning the interior structure of Pre-ACE13, warm ( $>10^{\circ}\text{C}$ ) and saline ( $>33.8$  psu) water shallower than 100 dbar located at 145.25°E–146°E existed as a warm-core ring above the thick remnant layer between 200 and 400 dbar ( $26.6$ – $26.7$   $\sigma_{\theta}$ ) at 145.7°E–146.3°E (Figures 5c and 5e). Both the surface warm saline ring (145.25°E–146.25°E) and the subsurface remnant layer (145.75°E–146.25°E) contained warmer and saltier waters than those in the western (northwestern) region of Pre-ACE13. Moreover, both layers had two horizontal temperature maxima around the periphery of Pre-ACE13, centered at 145.7°E and 146.2°E in the surface warm-core ring as well as the remnant layer. Beneath the remnant layer, cold freshwater between 400 and 500 dbar ( $26.7$ – $26.9$   $\sigma_{\theta}$ ) existed at 145.7°E–146.3°E as patchy extrema. Note that marked cold freshwater beneath the remnant layer was observed by floats from  $\sim 23$  May to July (Figures 4a and 4b), just after this observation. Slanting of the ACE to the west (northwest) with decreasing depth was indicated by the depressed peak of the isopycnals at middepths, near 146.1°E at 800 dbar and 145.8°E at 400 dbar. In contrast, upward-convex isopycnals at 147.1°E–147.8°E were represented in the RF1304 transect, which corresponded to the offshore side of the ACE (Figures 5d and 5f). Whereas the distributions of temperature, salinity, and isopycnals relative to the center of the ACE along the WK1305 transect were asymmetric, the meridional velocity distributions were relatively symmetric relative to the center of the eddy located at 146°E (Figure 5g). Both the zonal and meridional velocities between 145.5°E and 146.3°E were positively correlated with temperature at depths shallower than 500 dbar (Figure 5h). Although negative correlations between the velocities and temperature were also evident at 500–700 dbar, the heat transport  $\left( \int_{145.5^{\circ}\text{E}}^{146.3^{\circ}\text{E}} \rho C_p u' t' dx \left( \int_{145.5^{\circ}\text{E}}^{146.3^{\circ}\text{E}} \rho C_p v' t' dx \right) \right)$  indicated that the integrated values of these parameters at depths shallower than 500 dbar were far larger than those beneath this depth (Figure 5i). Here  $\rho$  is the density,  $C_p$  is the heat capacity,  $u'$  ( $v'$ ) is the zonal (meridional) velocity anomaly between 145.5°E and 146.3°E, and  $t'$  is the temperature anomaly between 145.5°E and 146.3°E at each depth. Therefore, northward and eastward heat transport due to the ACE during the shipboard observation was indicated.

Concerning the interior structure of ACE13 after the ship observations, cold water was observed at middepths (Figures 4a and 4e), and the occupation continued during P-2, when floats A and C were located near the center of the northward-propagating ACE13. The  $26.7$ – $26.8$   $\sigma_{\theta}$  density layer was obviously thicker than before this appearance of cold water. Composite sections obtained by data from three floats showed thick aligned cores beneath the region  $-20$  to  $20$  km from the center of the ACE (Figures 6a and 6b), the remnant core at depths of 200–400 dbar ( $26.6$ – $26.7$   $\sigma_{\theta}$ ), and the cold fresh core at 400–600 dbar ( $26.7$ – $26.9$   $\sigma_{\theta}$ ). In addition to the cold water appearance observed by the near-core floats, prominently cold and fresh water patches with a vertical scale of 50 m or less were frequently observed at depths of 100–400 m by float B, which typically rotated on the periphery of ACE13 from June to July (Figures 4c and 4d). For example, cold ( $<2^{\circ}\text{C}$ ) and fresh ( $<33.2$  psu) waters were frequently observed at densities of  $26.5$ – $26.8$   $\sigma_{\theta}$  (150–400 m) in early June.

During the stalled period, P-3, the remnant layer and the cold fresh core became thinner and more elongated than during P-2 (Figures 6c and 6d). The time series from individual profiles showed that a weak vertical salinity minimum around 200 dbar was observed in addition to the deeper temperature-salinity minimum around 400 dbar (Figures 4b, 4d, and 4f). The temperature ( $4$ – $5^{\circ}\text{C}$ ) and salinity ( $33.5$ – $33.6$  psu) at this shallower salinity minimum were obviously greater than those reported by Ueno and Yasuda [2005], as the remnant layer of the winter mixed layer was formed in the subarctic region ( $2$ – $3^{\circ}\text{C}$  and  $33.2$ – $33.4$  psu, respectively, around  $41^{\circ}\text{N}$ – $42^{\circ}\text{N}$ ,  $146^{\circ}\text{E}$ – $147^{\circ}\text{E}$ ), in spite of the similar density range ( $26.6$ – $26.8$   $\sigma_{\theta}$ ). Therefore, this shallower salinity minimum was likely a mixture of subarctic and subtropical water.

During the eastward-propagating period, P-4, composite profile sections indicated that the thickness of the remnant layer and the cold core in the  $26.7$ – $26.9$   $\sigma_{\theta}$  layer decreased to almost 150 and 100 m, respectively (Figures 6e and 6f). The salinity in the remnant layer also became fresher than in April. During P-4, the time series obtained by floats B and C indicated that prominent cold fresh waters again intermittently occurred around the remnant layer. For instance, float C observed markedly cold ( $<2^{\circ}\text{C}$ ) and fresh water ( $<33.2$  psu) at  $26.3$ – $26.7$   $\sigma_{\theta}$  (50–300 dbar) at around 15 September (Figures 4e and 4f). Moreover, prominently cold-water patches ( $<2^{\circ}\text{C}$ ) were also intermittently detected by float B at  $26.7$ – $26.8$   $\sigma_{\theta}$  from early to mid-September (Figure 4c). In addition to these patchy cold freshwater occurrences, in late-October, the disappearance of the saline layer at  $<100$  dbar was observed because of the development of a mixed layer that contained fresher water.

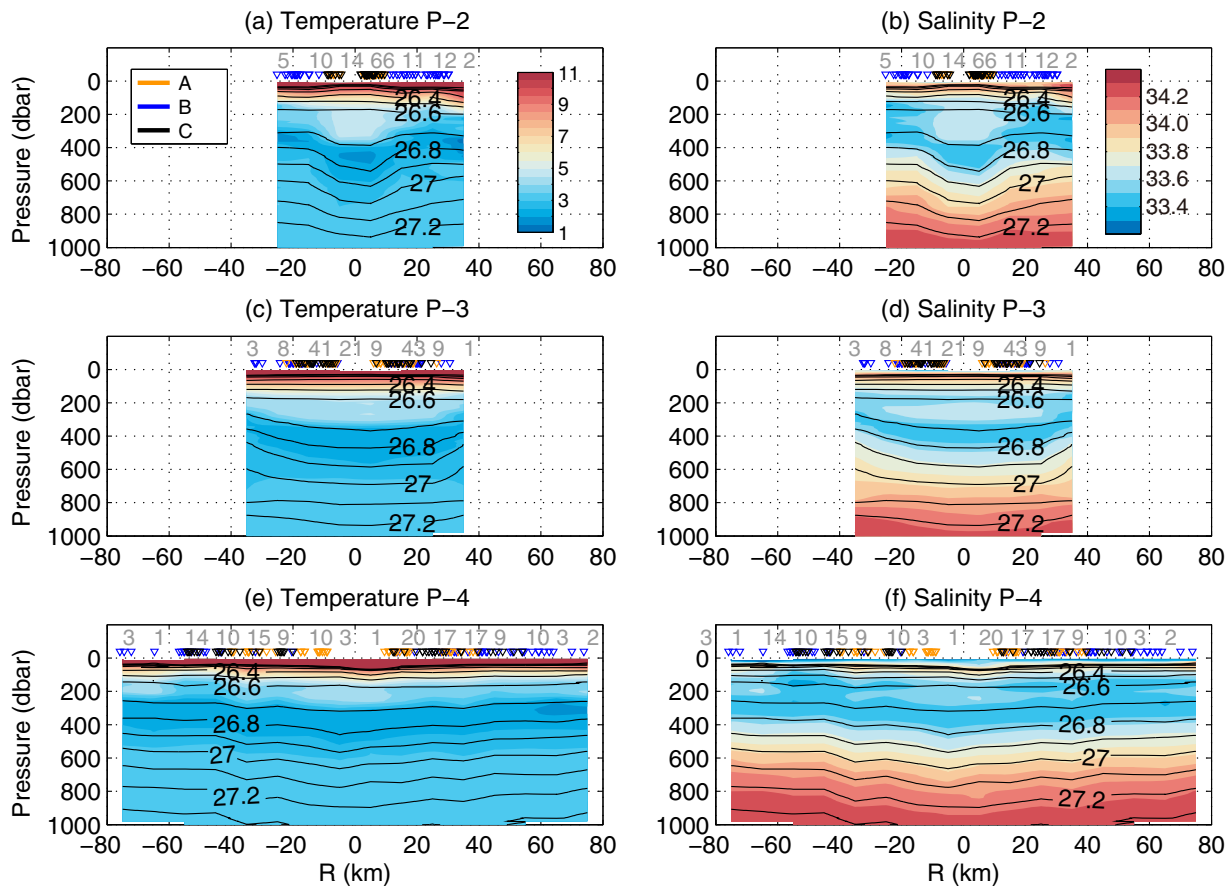


**Figure 6.** Vertical composite sections in the radial direction averaged horizontally in each 10 km bin. Separate averages are shown for values north and south of the center of the ACE, where north is positive. The left (right) column is temperature (salinity). The contours denote potential density. Number of profiles in each bin are shown above the plot.

The temperature and salinity of the remnant core during P-4 decreased compared with P-2. Indeed, the T-S diagram demonstrated decreases in temperature (salinity) at 26.6–26.7  $\sigma_\theta$  from  $\sim 4.9^\circ\text{C}$  ( $\sim 33.7$  psu) during P-2 to  $\sim 4.2^\circ\text{C}$  ( $\sim 33.55$  psu) during P-4, and these values are between the range of subarctic and subtropical properties (Figure 7). In contrast, an increase in temperature (salinity) at 26.7–26.8  $\sigma_\theta$  that corresponded to the cold core was observed and ranged from  $\sim 2^\circ\text{C}$  ( $\sim 33.4$  psu) during P-2 to  $\sim 2.5^\circ\text{C}$  ( $\sim 33.45$  psu).

With respect to the timing of the changes in the interior structure from P-2 to P-4, the time series of the near-core water properties demonstrated midterm temporal changes associated with each period in addition to a general decreasing trend throughout the whole period (Figure 8). For example, it was clearly shown that drastic decreases in salinity at densities lighter than 26.7  $\sigma_\theta$  occurred between P-3 and P-4 (Figures 8a and 8b). A similar rapid change in properties was also recognized at 26.2–26.8  $\sigma_\theta$  between P-2 and P-3, showing a step-like decrease in salinity (except for 26.4–26.6  $\sigma_\theta$ , at which a remarkable increase occurred in contrast). As an example of the evaluation of the water modification rate, we showed that the evolution at 26.65  $\sigma_\theta$  corresponded to the core of the remnant layer (Figure 8c). Although salinity had a decreasing trend from P-2 to P-4 ( $-7.4 \times 10^{-4}$  psu  $\text{d}^{-1}$ ), step-like changes in salinity were clearly indicated between P-2 and P-3 and between P-3 and P-4. Therefore, the timing of the change in the ACE13 movement generally corresponded to that of the change in the interior water mass salinity.

### 3.3. Warm and Cold Water Appearances and Their Impact on Interior Structures and Water Properties

Based on the time series provided by the floats (Figure 4), during P-1, rapid profile changes were demonstrated at least twice. The first one occurred during the merging of Pre-ACE13 with another ACE pinched off

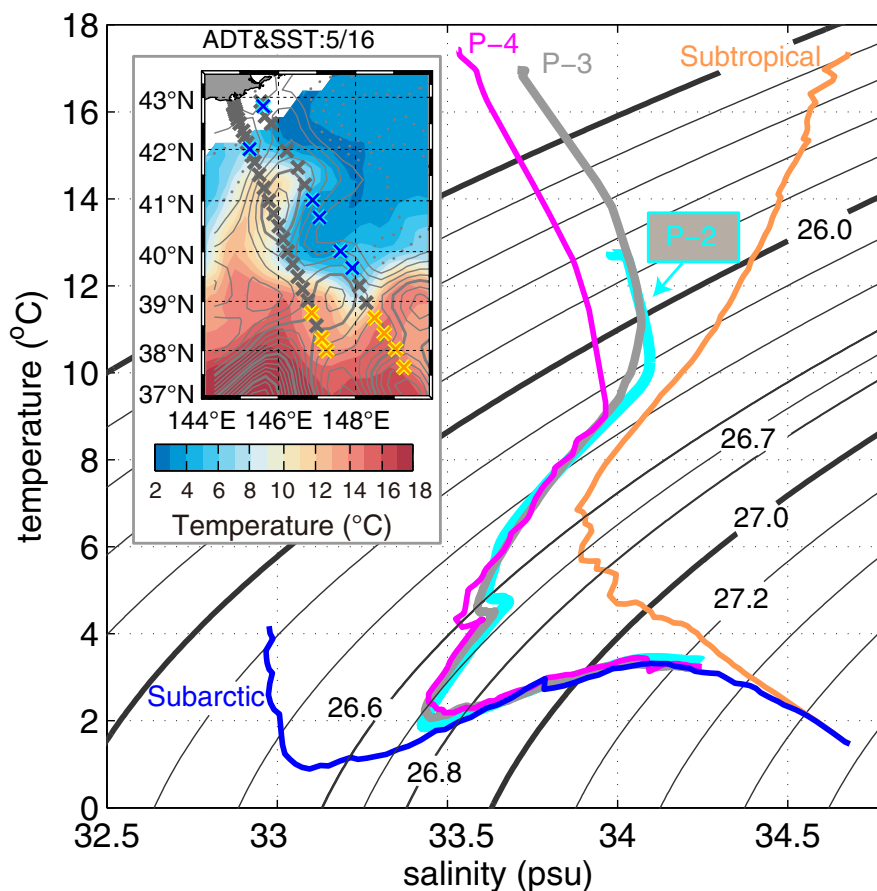


**Figure 7.** Temperature-salinity profiles. The profiles of P-2, P-3, and P-4 were the same as those shown in Figure 6. The profiles of subarctic and subtropical water were calculated from the shipboard observations represented in the small plot.

from the Kuroshio Extension in April, and the second was the encounter with subarctic water characterized by low temperature and salinity into middepths in May. The merge began in early April, just after the deployment of the floats (6 April) and lasted until almost late April (Figures 9a–9c). During this interaction, high-temperature and salinity water above the surface and winter mixed layer was rapidly isolated from the surface and recognized as the remnant layer (Figure 10).

After that, the second major change in the Pre-ACE13 structure was caused by the appearance of cold fresh subarctic water beneath the remnant layer that occurred in mid-May. This change in properties was triggered by the development of a northward-warm (southward-cold) tongue-like SST distribution (Figures 9d–9f), and it remained until July as the appearance of cold-water in profiles observed by floats A and C. Just after this appearance of cold-water, float D was detrained from Pre-ACE13 via the northern edge of Pre-ACE13 at the end of May, which was similar to the subsequent detrainment of floats from an ACE after cold-water intrusions as reported by Itoh *et al.* [2011a]. The time series obtained by float C indicated that the encounter with the cold freshwater at 400–500 dbar occurred beneath the southwest part of the ACE around 23 May, when its trajectory drastically changed and the radius of the float trajectory became markedly small (Figure 11). In addition to subarctic water at middepths, warm saline water also appeared near the surface (<100 dbar) in profiles from around 20 May. And then, the formation of ACE13 and its multilayer structure occurred: a near-surface warm-core ring, a subsurface remnant layer (warm core), and a middepth cold-core structure. It was noted that after the second event, the radius of the ACE was larger than before the event, although Itoh *et al.* [2014a] reported shrinking of the upper warm core after the intrusion of cold waters into middepths.

After the formation of the ACE13 as an isolated anticyclone, the time series of the near-core water properties showed a midterm temporal change associated with each period (P-2, P-3, and P-4), as mentioned

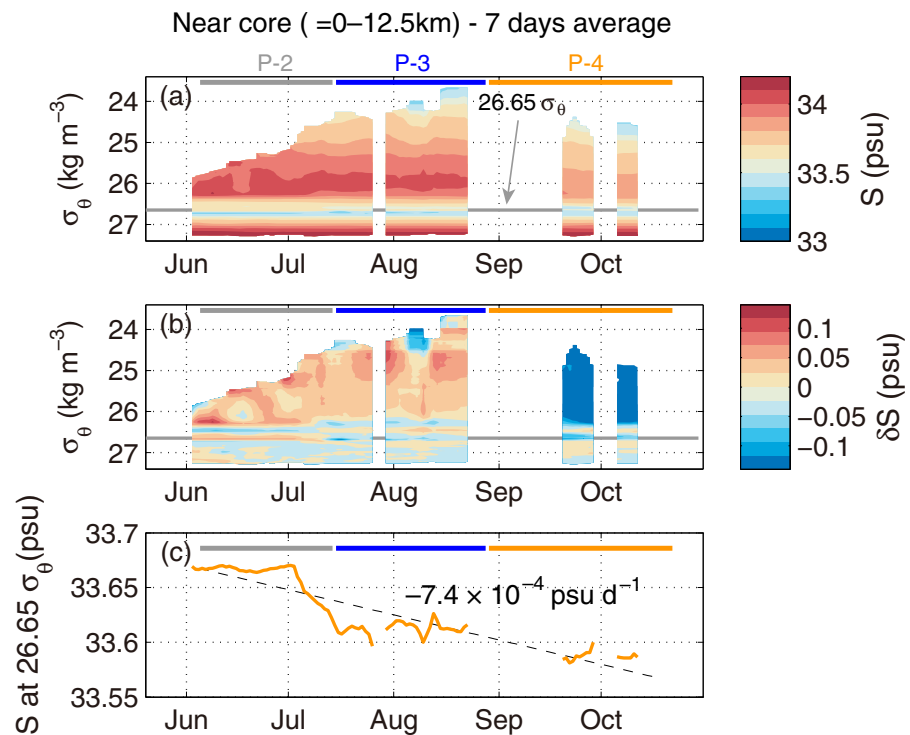


**Figure 8.** The evolution of salinity in the core of the eddy ( $R = 0\text{--}12.5$  km). (a) Isopycnal average. (b) Anomalies with respect to the averages over the entire observational period (from P-1 to P-4). (c) Anomalies at  $26.65 \sigma_\theta$  (core of the remnant layer).

above (Figure 8). The SST distribution indicated that just before the change from P-2 to P-3, cold water ( $<15^\circ\text{C}$ ) occurred near the northern periphery of the ACE13 at areas  $>42^\circ\text{N}$  and  $>146^\circ\text{E}$  (Figure 9g). In contrast, after the change from P-2 to P-3, warm water rapidly spread to the east of ACE13 around  $42^\circ\text{N}$ ,  $148.5^\circ\text{E}$  (Figures 9h and 9i). During this change, the trajectories of floats A and C elongated and that of B shrank. However, on 23 August, just before the change from P-3 to P-4, a relatively cold ( $19.5\text{--}20.5^\circ\text{C}$ ) SST distribution was found to reach near the center of ACE13, showing a tongue-shaped distribution near the southern edge of ACE13 (Figure 9j). After that, the trajectories of the floats rapidly separated and the SST within ACE13 got colder, from  $20.5\text{--}21^\circ\text{C}$  (Figure 9j) to  $19\text{--}19.5^\circ\text{C}$  (Figures 9k and 9l). The occurrences of the tongue-shaped SST distributions were similar to those during the interactions in P-1 (Figures 9a–9f).

### 3.4. Short-Term Variations in Temperature and Salinity as Observed by the Floats

As mentioned in section 3.2 (e.g., Figure 4), the oscillations of isopycnal surfaces with a period shorter than 20 days (especially  $\sim 10$  days) were correlated with the position of the floats relative to the ACEs (Figure 12). High-pass-filtered potential density at 500 dbar,  $\delta\rho$ , obtained with a Butterworth high-pass filter with a half-power of 20 days, and high-pass filtered latitude of ascending float positions,  $\delta y$ , showed a significant negative correlation ( $r = -0.33$ ,  $p < 0.01$ ), especially when the floats were in the ACEs (Figures 12a and 12b). In contrast, float D did not show clear relationships between  $\delta\rho$  and float position after June, when the float was detained from ACE13 (Figure 12c). The high-passed potential density at 500 dbar,  $\delta\rho$ , also had a significant positive correlation with longitude ( $r = 0.12$ ,  $p < 0.01$ ; data not shown). These results suggested denser water tended to be distributed in the southeast to the center of ACE13. As an example, Figure 13 clearly shows the horizontal distribution of the positive density anomaly at 500 dbar in the southeastern part of ACE13.

The time series of the correlations between 20 day high-passed density and position (represented in complex number form) indicated that increases in the correlation coefficients ( $r$ ) generally occurred at depths of  $>350$  dbar, and changes in direction from north in a clockwise manner ( $\Phi$ ) were related to behavior modulations of ACE13 (Figure 14). For example, a clear change in  $\Phi$  from  $180^\circ$  (southward) to  $270^\circ$  (westward) was recognized during the period from mid-May to early June (Figure 14b). After this change,  $r$  drastically decreased once, and  $\Phi$  was around  $135^\circ$  (southeast). The timing of this drastic change corresponded to the timing of the ACE13 isolation from the Kuroshio Extension. Similar drastic changes in  $r$  and  $\Phi$  were observed

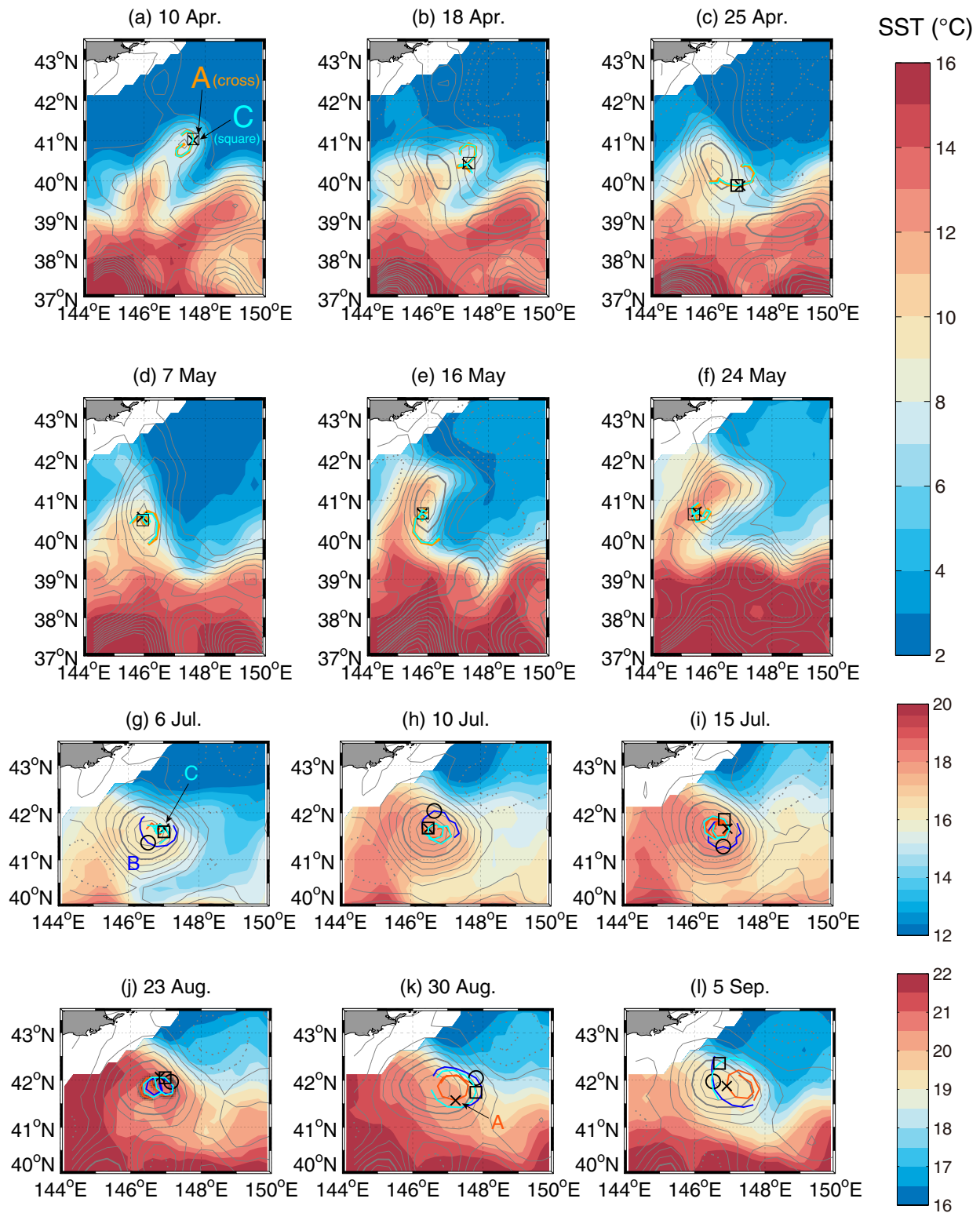


**Figure 9.** Snapshots of sea surface temperature (SST, color shading) and absolute dynamic topography (ADT, contours). (a–f) During interactions (P-1). The circles and white lines denote the position of float A’s ascent and its trajectory 5 days before and after, respectively. (g–i) From P-2 to P-3. (j–l) From P-3 to P-4.

in late August, when the modulation from P-3 to P-4 was recognized. In contrast to the corresponding changes between ACE13 movement and the indicators ( $r$  and  $\Phi$ ), from mid-June to mid-July (northward P-2) and during September (early eastward P-4),  $\Phi$  showed a unidirectional pattern around  $135^\circ$  from north

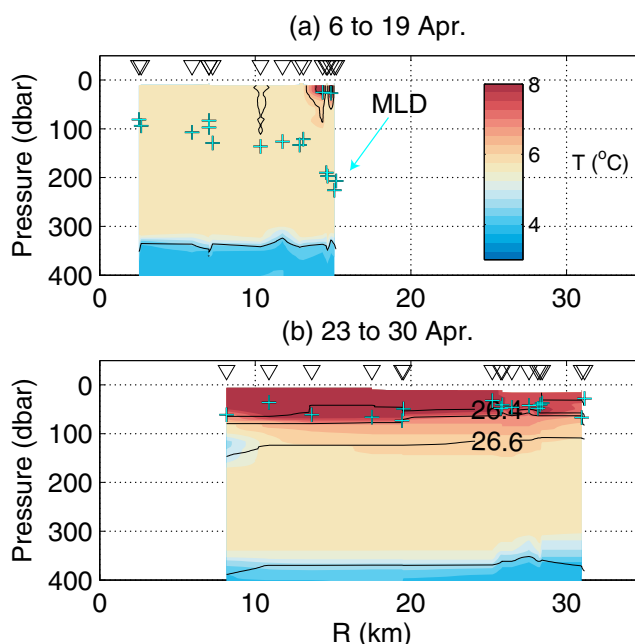


**Figure 10.** Vertical sections of temperature in the radial direction. (a) From 6 to 19 April before the first interaction. (b) From 23 to 30 April after the first interaction. The crosses represent the mixed layer depth (see section 2). The triangles above the sections denote the positions of the profiling floats. The contours represent potential density.

(i.e., southeast) (Figure 13b). The vertical average of  $\Phi$  at 350–700 dbar,  $\bar{\Phi}$ , clearly indicated the direction orthogonal (southeast) to the isobaths, especially during the northward P-2 and eastward P-4 periods (Figure 15a). In contrast to this unidirectional density anomaly pattern,  $\bar{\Phi}$  during the stalled P-3 period varied from southeast to southwest from early to mid P-3, and was directed east in late P-3 (Figure 15b). The center of ACE13 was generally located within 150–200 km of the 500–1000 m isobaths.

## 4. Discussion

### 4.1. Temporal Changes in Observed Profiles Around Pre-ACE13

In the above sections, we examined temporal changes in the structure and water mass of the long-term eddy and investigated the relationship between the eddy propagation pattern and its interior structure. Floats deployed in an eddy can move toward another eddy due to eddy-eddy interactions and the wave-like behavior of the eddy (e.g., linear Rossby waves) when the ratio of the orbital velocity of the eddy to its propagating speed is small [e.g., Ichikawa *et al.*, 1995; Ebuchi and Hanawa, 2001]. Thus, we discuss below the temporal changes in structure before the isolation of ACE13 (i.e., Pre-ACE13 during P-1), when some active interactions between eddies were recognized.

In addition to the lower magnitude of the geostrophic velocity averaged within Pre-ACE13 during P-1 compared with that during P-2 to P-4, a drastic decrease in the magnitude over several days occurred as a subevent during the second half of April (Figure 3d). The temporal changes in profiles around Pre-ACE13 occurred as drastic short-term events over periods from a couple of days to 10 days, showing warm saline water at the surface in April. During this event, the floats appeared to move toward another ACE located southwest of the eddy in which the floats were deployed (e.g., Figures 9a–9c). Therefore, the profile changes recorded by the floats are likely to be associated with weakening of the geostrophic velocity caused by rapid interactions between ACEs aligned north–south, rather than the propagation of linear Rossby waves aligned east–west. During these interactions, the satellite data show a tongue-shaped intrusion of warm water spread over both eddies at the surface, suggesting a merger between them (Figures 9a–9c). Such interactions and subsequent merger have previously been reported in this region [e.g., Yasuda *et al.*, 1992]. The entrainment of warm and saline water in April could move the surface mixed layer to

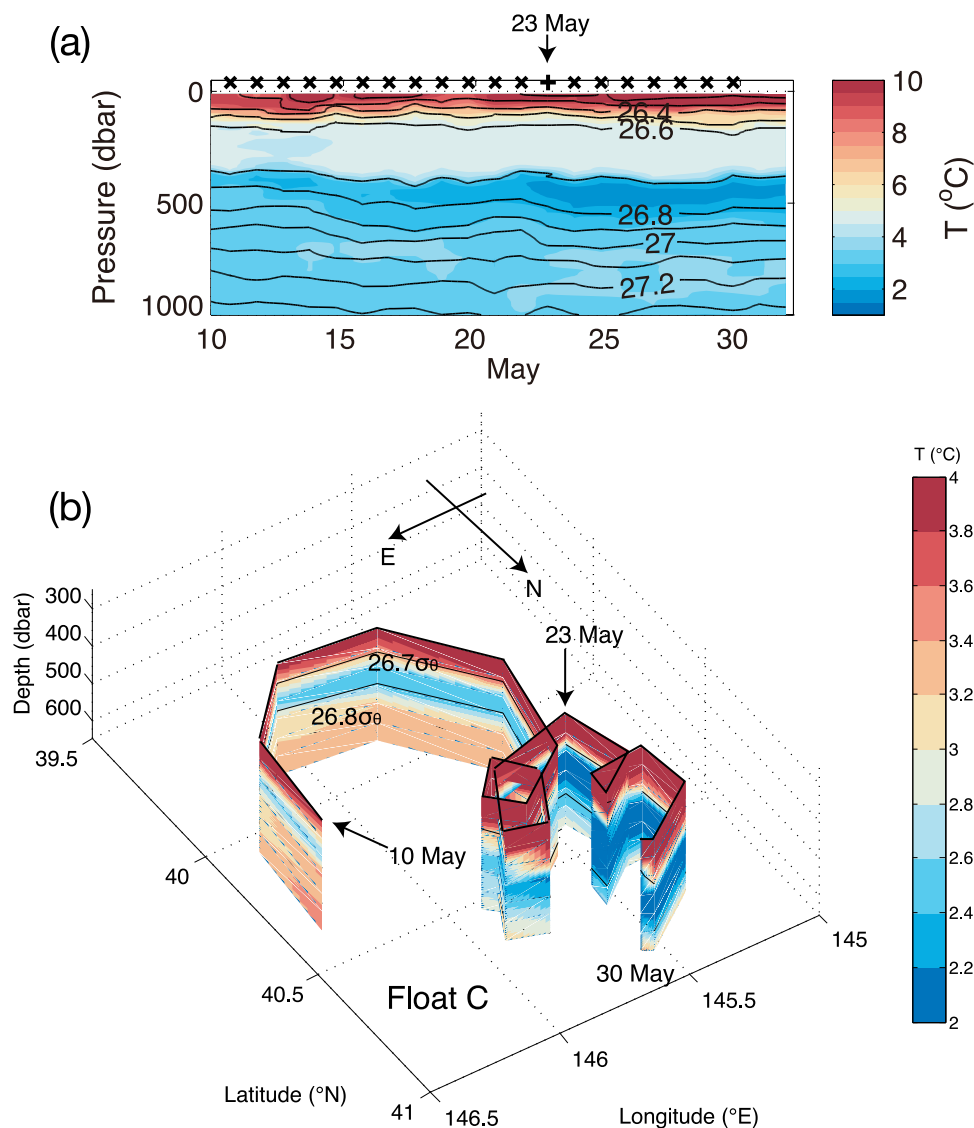


**Figure 11.** Time series sections of float C around the occurrence of a thick cold freshwater intrusion. (a) Same as Figure 4e but from 10 to 31 May. (b) A 3-D display of Figure 11a focused at depths of 350–550 dbar.

shallower depths. Thus, such intrusions near surface are regarded as a positive lateral buoyancy flux from the south and may determine the timing of regional blooms [e.g., Shiozaki *et al.*, 2014].

During the event in May (Figures 9d–9f), we again found tongue-shaped intrusions of warm water in Pre-ACE13 at the surface. In addition to the surface, WK1305 revealed the formation of structures, including patches of cold freshwater, at middepth beneath the mesoscale eddy (145.25°E–146.5°E; Figures 5a, 5c, and 5e). Thus, the appearance of cold water can also be interpreted as an intrusion at middepths. The magnitude of the geostrophic velocity rapidly decreased again from early-May to mid-May (Figure 3d). In addition, it became difficult to detect the eddy based on the Okubo-Weiss parameter,  $W$ , in mid-May (Figure 3d) in spite of the obvious ADT structure (Figure 9e), suggesting that deformation was dominant over rotation. Therefore, the decrease in the magnitude of the geostrophic velocity associated with the interactions and/or deformation may have led to the intruded patches at middepths in the eddy and to detrainment of the floats (e.g., float D).

According to float C and the ADT from 23 May (Figures 9d–9f and 11b), thick cold water appeared at mid-depths beneath the southwest part of the eddy after the decrease in the magnitude of the eddy's

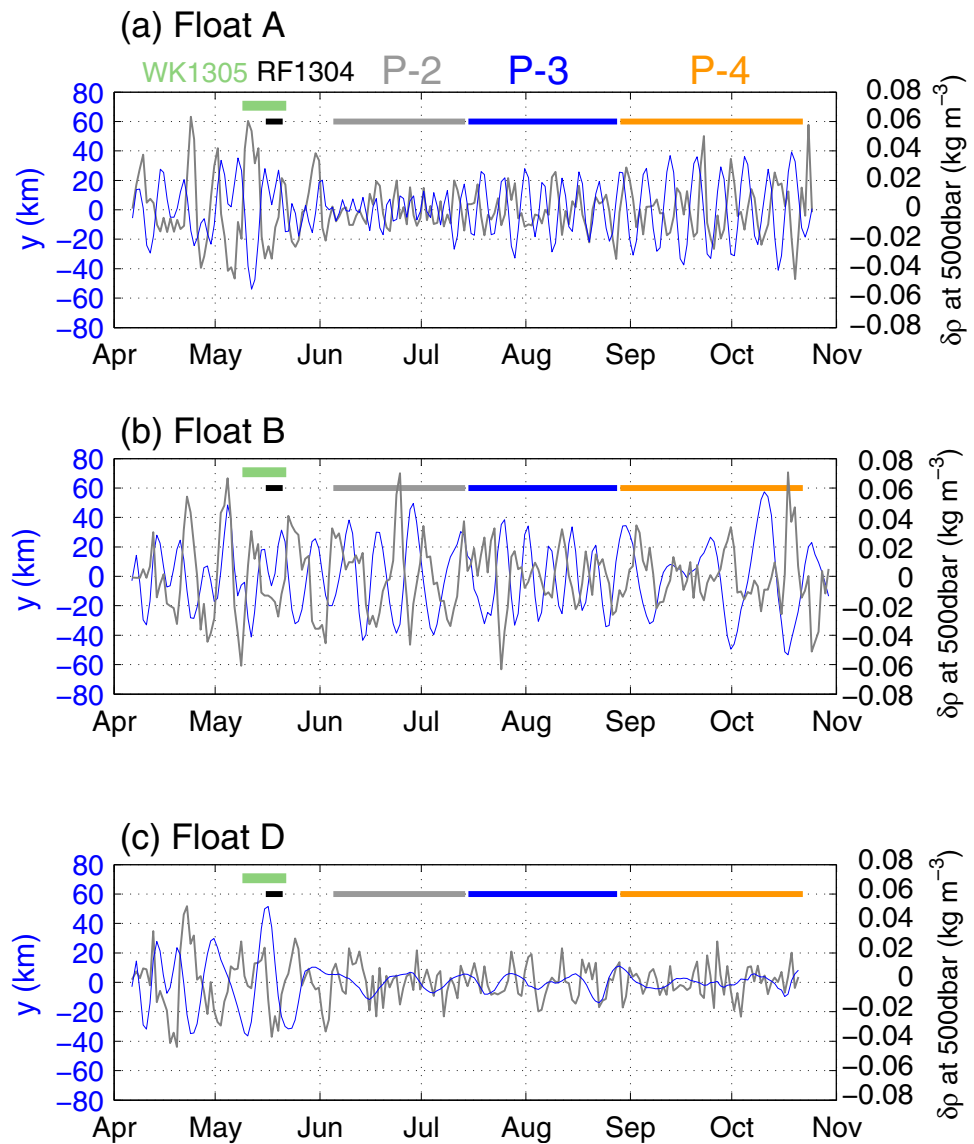


**Figure 12.** Time series of the 20 day high-pass filtered potential density anomaly at 500 dbar,  $\delta\rho$ , and latitude position of each float relative to the center of the eddy,  $y$ , obtained from data of (a) float A, (b) float B, and (c) float D.

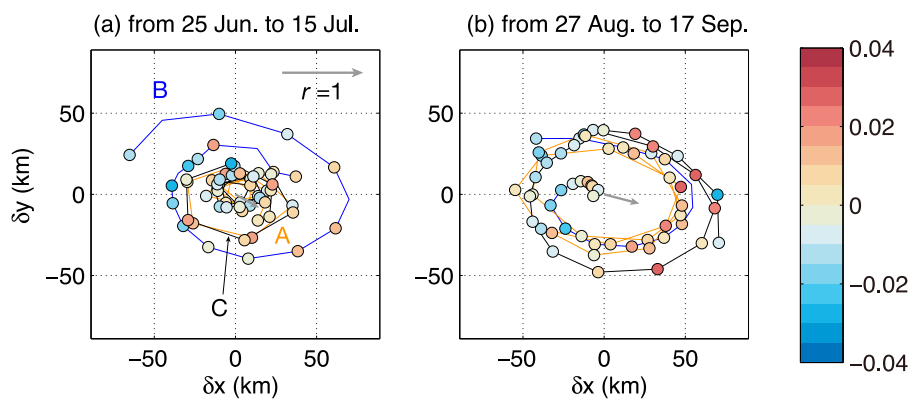


**Figure 13.** Examples of the horizontal distributions of the 20 day high-pass filtered density anomaly at 500 dbar relative to the 20 day high-pass filtered locations of the floats during (a) northward P-2, and (b) eastward P-4. Length and direction of gray arrow denote the magnitude and the direction of the correlation coefficient,  $r$ , in complex planes.

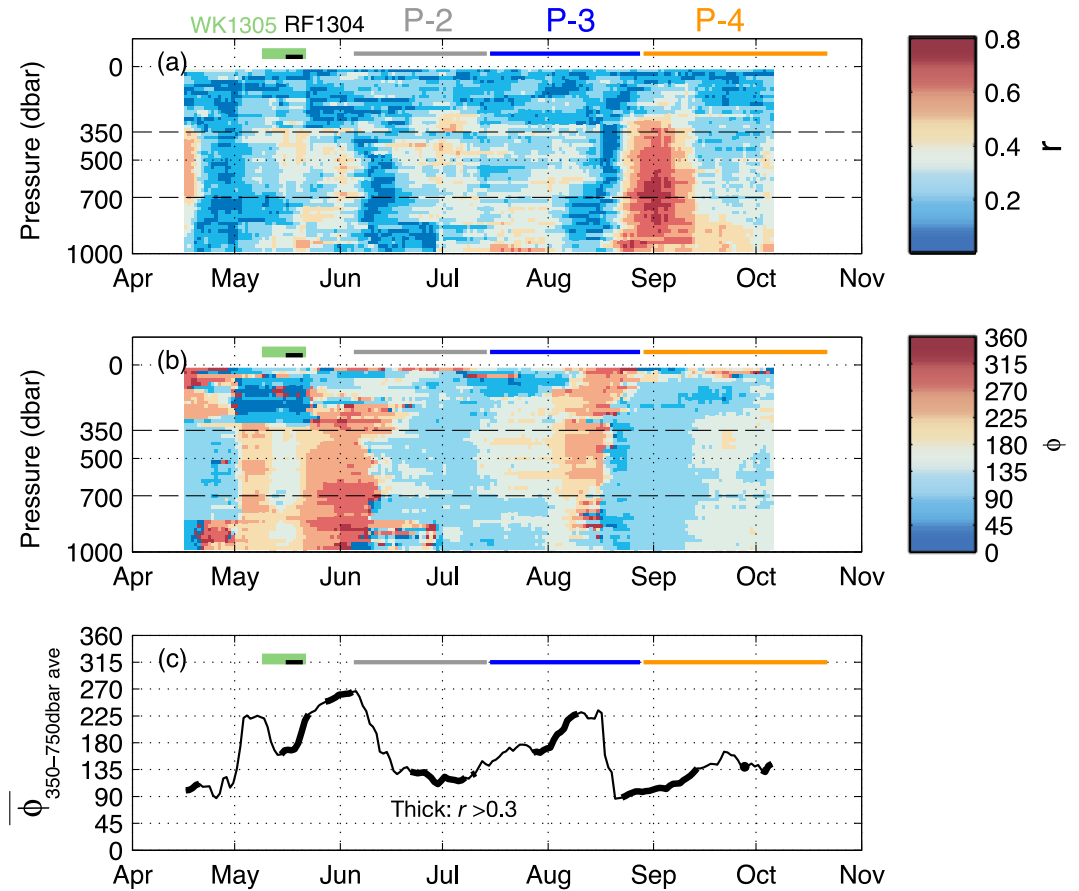


**Figure 14.** The evolution of the maximum correlation coefficient between the horizontal displacement of the float and density anomaly at 500 dbar in complex planes,  $r$ , and the direction of  $r$  in the complex plane,  $\Phi$ . (a) Vertical section of  $r$ , (b) vertical section of  $\Phi$ , and (c) vertical average of  $\Phi$  at depths of 350–700 m,  $\bar{\Phi}$ . The thick line in Figure 14c denotes  $r > 0.3$ .

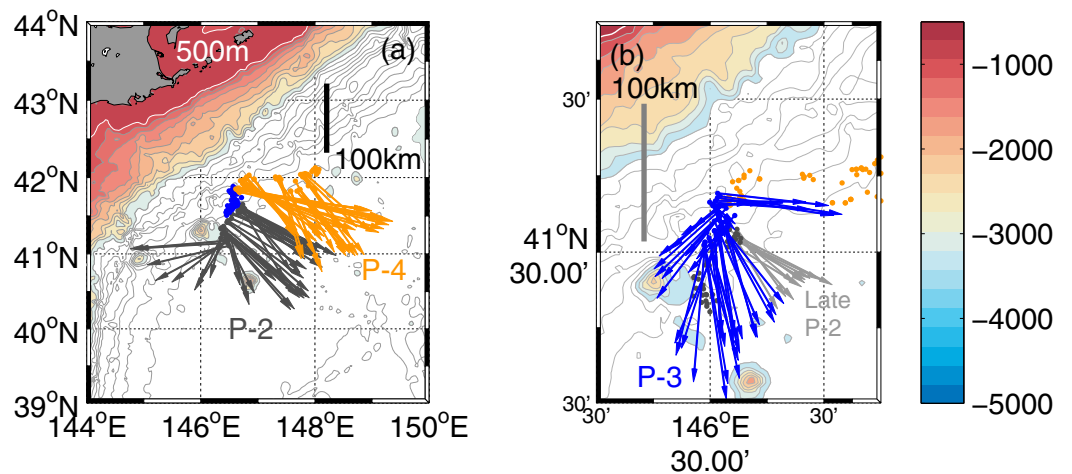


**Figure 15.** Horizontal vector representation of Figure 13c vertically averaged over 350–700 dbar superimposed on the topography. The colors of the circles at the base of the arrows correspond to each period during (a) P-2 and P-4 and (b) P-3. For comparison, vectors during late P-2 (last 10 days) are also represented in Figure 15b as light gray arrows. The isobath interval is 500 m. The 500 m isobath is shown in white.

geostrophic velocity (Figure 3d). In spite of drastic changes in its orbit around 23 May, float C generally stayed within the mesoscale eddy after this time (e.g., Figure 9f), until P-2. In addition, the thick cold water remained near the center of ACE13 until July (Figures 4a and 6a). Thus, rapid entrainment of thick cold water into middepths (beneath the remnant layer) is likely to have occurred [e.g., Itoh *et al.*, 2014a], although the faster movement of the ACE center due to interactions, relative to the floats' orbital velocity, sometimes led to pseudovariations in the time series.

In contrast to the decreasing trend during the first half of May, the magnitude of the mean geostrophic velocity within the eddy increased from mid-May to June (Figure 3d). In addition, enlargement of the eddy's radius, especially in the longitudinal direction, is apparent from the ADT data (Figure 3a). Ueno *et al.* [2009, 2012] suggested that along the Alaskan Stream near 170°W, eddies sometimes intensified possibly due to the outflow of low-potential vorticity water from the Bering Sea. The similar amplification and regeneration of ACEs by low-potential vorticity waters from the Sea of Okhotsk was reported around the Kuril Islands [Yasuda *et al.*, 2000; Itoh *et al.*, 2014a]. Although the floats were distant from the Sea of Okhotsk (40°N–41°N) in May, the thick cold-water intrusion and the subsequent enlargement of ACE13b was similar to intensification reported in previous studies [e.g., Yasuda *et al.*, 2000].

In the present study, it was suggested that the rapid decrease in the magnitude of the orbital velocity, compared with the propagating speed and/or deformation of the eddy, may have led to rapid inside/outside water mass exchanges (from a couple of days to ~10 days). However, we should pay attention to the horizontal resolution of AVISO (1/4°) and the accuracy of the orbital velocity estimations from floats that generally flowed at middepths. These factors could have caused uncertainty concerning the propagation speed and orbital velocity (including geostrophic velocities within the ACE). To understand such exchanges relative to the mesoscale features of an eddy, further studies are required based on position-controlled observations relative to the eddy (e.g., glider time series and gridded shipboard transects), more accurate estimations of orbital velocity via surface drifter buoys, and eddy-resolved numerical models that can provide a snapshot of the eddy's structure and its temporal changes.

#### 4.2. Temporal Changes and Variability in the Water Mass Within ACE13

The multilayer structure of ACE13 (i.e., the thick cold freshwater intrusion) could have contributed to the gradual modification of the water mass near the center of ACE13 via vertical interactions by cooling the upper warm saline layer. Despite the ambient subarctic water, increases in the temperature and salinity at the cold core from P-2 to P-4 (Figure 7) suggested a downward positive temperature and salinity flux from the remnant layer. Salt-finger convection was responsible for these fluxes, similar to the observations reported by Saito *et al.* [2011] concerning the Transition Region Mode Water at the 26.4–26.6  $\sigma_\theta$  layer and the above layer. Salt-fingering between vertically aligned layers might play an important role in the rapid modification of North Pacific Intermediate Water (NPIW) in addition to salt-finger convection caused by lateral mixing between subtropical and subarctic waters at densities lower than 26.8  $\sigma_\theta$  (the core density of NPIW) [Talley and Yun, 2001].

In addition to the gradual modification of the water mass in the ACE13, the rapid change in salinity near the center (0–12.5 km) might also be related to the water mass modification (Figure 8c). From P-2 to P-4, we found that the timing of the change in the ACE13 movement generally corresponded to that of the change in the interior salinity (Figure 8c). Based on the drastic change in the SST distribution around ACE13 (Figures 9g–9l), we presume that exchanges of water masses along the edge of ACE13 occurred. As the interior changes occurred after the enlargement of the cold front at the northern side of ACE13 (Figure 9g) and the cold-tongue-shaped distribution in the center of ACE13 (Figure 9j), interactions between the poleward-propagating ACE and ambient waters, such as Oyashio water, would be expected. These interactions along the edge, including submesoscale disturbances [Shcherbina *et al.*, 2010], could change the interior structures and contribute to water mass modifications within ACE13. Although the causes of the drastic export of water from the center of ACE13 are unclear, the rapid decrease in the magnitude of the geostrophic velocity during mid-September (Figure 3d) might be related to these interactions.

#### 4.3. Temporal Changes in Interior Structures and Propagating Pattern of ACE13

We demonstrated significant relationships at 500 dbar between horizontal density anomalies and high-pass-filtered longitude and latitude, with negative and positive correlation coefficients, respectively (see

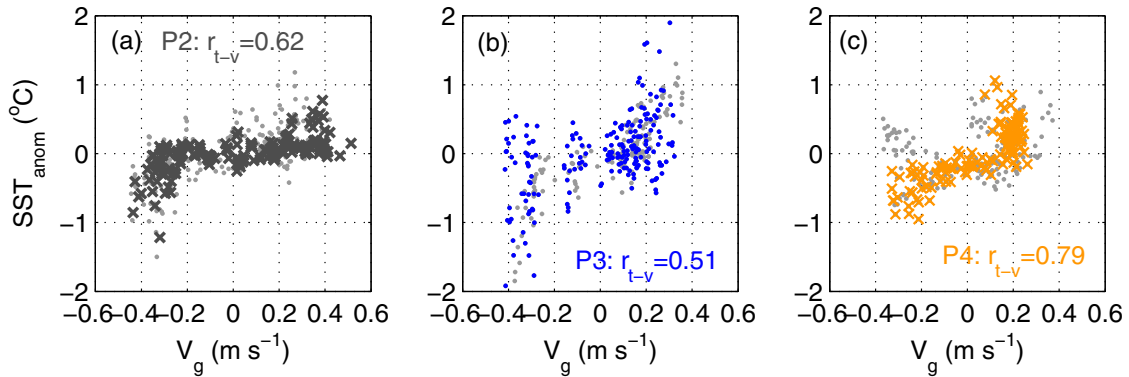


**Figure 16.** Relationships between northward geostrophic velocity and sea surface temperature anomalies along the east-west transect of ACE13. The definition of the center and area of ACE13 are given in section 2. Highlighted points denote days for which  $r > 0.3$  ( $< 0.3$ ) in Figure 14b during P-2 and P-4 (P-3). Another correlation coefficient,  $r_{t,v}$ , is calculated from the highlighted points. The geostrophic velocity data and sea surface temperature data are from AVISO and GHRSSST, respectively (see section 2).

section 3.4). Assuming that the float positions recognized at the surface were attributed to velocities at 500 dbar, these significant relationships suggested that the trajectory relative to the center of ACE13 crossed isopycnal contours at 500 dbar, showing a tendency toward the distribution of lighter densities near the shore in the cross-trench direction (Figure 13). We presumed that the reason for the trajectory crossing the isopycnals at 500 dbar was the vertical slanting of the vortex and isopycnals in the offshore side of the ACE that were shallower than those in the nearshore side relative to the axis of the ACE (e.g., the  $27.0 \sigma_\theta$  isopycnal in Figure 5d). This interpretation of the tilting of the ACE was reinforced by shipboard observations (Figures 5a and 5b). A similar tilting of ACEs northward and westward toward the trenches was reported by *Itoh and Yasuda* [2010b, Figure 14]. In addition, the upward cyclonic isopycnals east of the ACE obtained during the RF1304 cruise (Figures 5c and 5d) were similar to those reported by *Itoh and Yasuda* [2010b].

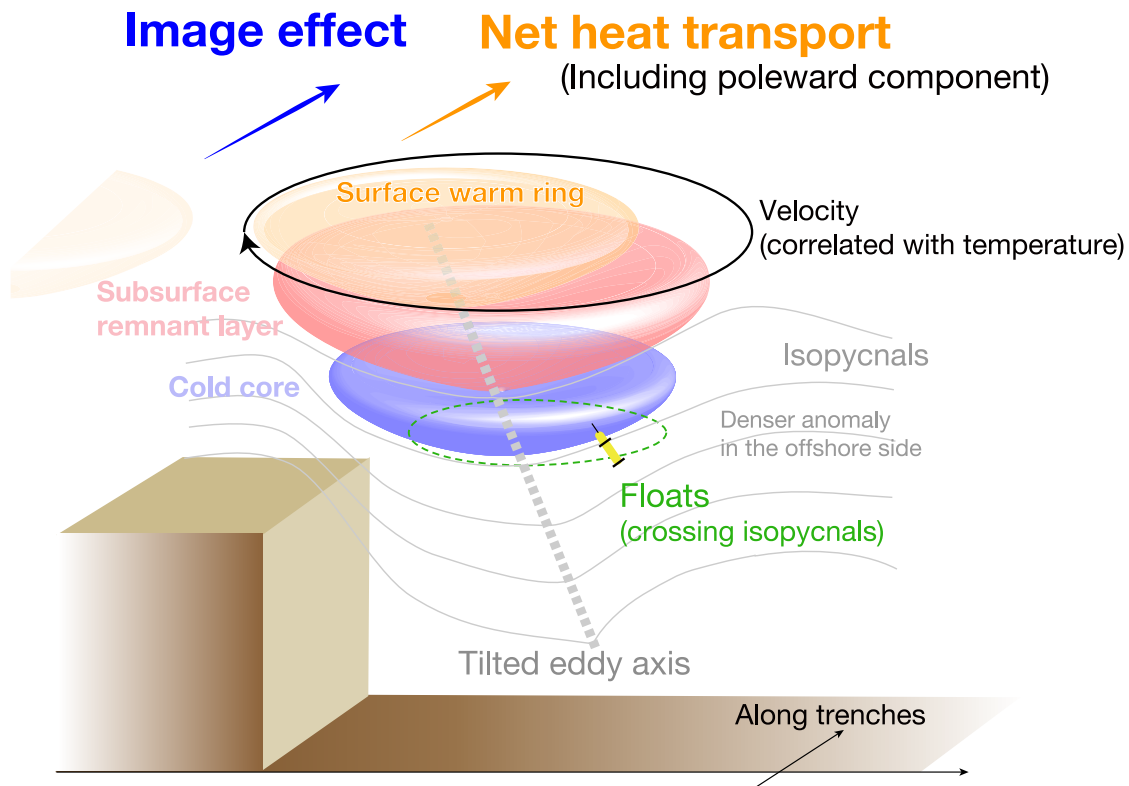


**Figure 17.** A schematic diagram of the correspondence between the interior structure and poleward movement of ACE13.

The clear southeast-unidirectional pattern of  $\bar{\Phi}$  suggested tilting of the vortex tube on the steep slope of the trenches during the northward P-2 and eastward P-4 periods (Figure 15). In contrast, during the stalled P-3 period,  $\bar{\Phi}$  indicated directions varying from southeast to southwest. Therefore, we can conclude that the ACE13 movement was very sensitive to local topography, probably through the tilting of the vortex tube. This tilting of ACE13 toward the topography was consistent with the compression of an ACE due to steep slopes, as reported in previous numerical studies [Itoh and Sugimoto, 2001; Sutyryn et al., 2003; Hyun and Hogan, 2008], which emphasized that the image effect could result in poleward movement of ACEs.

Although the physical processes that caused the changes in the direction of the eddy's tilt are unclear, in addition to topographic effects, such changes could result from disturbances triggered at the eddy's periphery due to ambient currents and other eddies. For example, from late May to early June, a drastic change in  $\bar{\Phi}$  occurred (Figure 14c) in conjunction with prominent cold and fresh water located in the outer part of the ACE, as observed at 100–400 dbar by float B, although a temporally solid remnant layer was detected near the center by float A (Figure 4). Thus, interactions with cold water along the edge of the ACE might have contributed to the change in  $\bar{\Phi}$ .

#### 4.4. Role of ACE Interior Structures in Poleward Movement and Heat Transport

The poleward net heat transport of the tilting ACE due to the correlation between temperature and velocity [Roemmich and Gilson, 2001] also allowed ACE13 to move northward because of the poleward propagation of the gravity center of the warm core. According to the WK1305 transect, the positive heat transport at depths shallower than 500 dbar was more extensive than the negative transport at 500–700 dbar (Figure 5i). This result indicates that the net heat transport to the northeast was associated with the tilting of ACE13. Similar correlations were observed during P-4 based on the horizontal velocity derived from the ascending position of the floats (data not shown). Moreover, daily data during P-2 and P-4 show clear positive correlations between the SST anomalies along the east–west transects through the center of ACE13 and the meridional geostrophic velocity along the transects (Figure 16). In contrast, the relationships between the SST anomalies and geostrophic velocity during P-3 were more variable (Figure 16b). Therefore, the results provided by the satellite data are consistent with the enhancement of net northward heat transport during P-2 and P-4, and the subsequent poleward propagation of the warm core's gravity center due to transport during these periods.

In conclusion, we proposed that the tilting of the ACE toward the steep slope of the trenches functioned as an efficient poleward transport mechanism for heat and materials because of the net heat transport resulting from the ACE's tilting structure [Roemmich and Gilson, 2001; Qiu and Chen, 2005] and the poleward movement of the ACE itself from the image effect [Itoh and Sugimoto, 2001; Sutyryn et al., 2003; Hyun and Hogan, 2008]. This model of effective poleward heat transport is consistent with features of the eddy corridor [Itoh and Yasuda, 2010a]. In addition, we also demonstrated the transport exhibited 1–2 month variability associated with changes in the interior structure of the ACE. Poleward movements of ACEs are probably affected by background flows, such as the Oyashio current; however, interior structures of ACEs, such as unidirectional density anomaly patterns, also contribute to transport and modifications of water masses. Figure 17 shows a schematic diagram depicting the correspondence between eddy structure and propagation. More research is required to understand this relationship, including the influence of currents (e.g., the northeastward return flow of the Oyashio [e.g., Isoguchi and Kawamura, 2006]), anticyclonic barotropic circulation around the rise in the region of 40°N–40.5°N, 145°E–147°E (including the Neptune effect; H. Nishigaki, personal communication, 2015), and the pseudo  $\beta$  effect [e.g., Yasuda et al., 2000] on the behavior of poleward ACEs. Poleward ACEs could also affect intermediate gyre transport in the North Pacific, surface circulation, and the formation of NPIW through intergyre movement via various water-mass intrusions, modification of the water masses (e.g., vertical processes such as salt-fingers), and exchanges of water masses at higher latitudes.

#### References

- Boebel, O., J. Lutjeharms, C. Schmid, W. Zenk, T. Rossby, and C. Barron (2003), The Cape Cauldron: A regime of turbulent inter-ocean exchange, *Deep Sea Res., Part 1*, 50, 57–86, doi:10.1016/s0967-0645(02)00379-x.
- Byrne, D. A., A. L. Gordon, and W. F. Haxby (1995), Agulhas eddies—A synoptic view using Geosat ERM data, *J. Phys. Oceanogr.*, 25, 902–917, doi:10.1175/1520-0485(1995)025<0902:AEASVU>2.0.CO;2.
- Chelton, D. B., M. G. Schlax, R. M. Samelson, and R. A. de Szoeke (2007), Global observations of large oceanic eddies, *Geophys. Res. Lett.*, 34, L15606, doi:10.1029/2007GL030812.

#### Acknowledgments

The data from floats B and D are available from the Earth Surface system Dynamics Database of Atmosphere and Ocean Research Institute, University of Tokyo, Center for Earth Surface system Dynamics (<http://cesd.aori.u-tokyo.ac.jp/cesddb/data.html>). Data from floats A and C were deployed by Japan Agency for Marine-earth Science and Technology (JAMSTEC) as parts of the Western North Pacific Integrated Physical-Biogeochemical Ocean Observation Experiment (INBOX) intensive observations of an Anti-Cyclonic Eddy (ACE-INBOX), and also made freely available by the International Argo Program and the national programs that contribute to it (<http://www.argo.ucsd.edu>, <http://argo.jcommops.org>). The Argo Program is part of the Global Ocean Observing System. The hydrographic data obtained by the R/V *Wakataka-maru* and R/V *Ryofu-maru* are available by the Tohoku National Fisheries Research Institute ([http://trfri.fra.affrc.go.jp/seika/a-line/a-line\\_index.html](http://trfri.fra.affrc.go.jp/seika/a-line/a-line_index.html)) and the Japan Meteorological Agency (<http://www.data.jma.go.jp>), respectively. We thank E. Oka and the captain, officers, and crew of the R/V *Hakuhoh-maru* for deployment of the four floats. We also thank R. Inoue, V. Faure, H. Nishigaki, and D. Itoh for their fruitful suggestions. This study was supported by The New Ocean Paradigm on its Biogeochemistry, Ecosystem, and Sustainable Use (NEOPS).

- Cheng, Y. H., C. R. Ho, Q. N. Zheng, and N. J. Kuo (2014), Statistical characteristics of mesoscale eddies in the North Pacific derived from satellite altimetry, *Remote Sens.*, *6*, 5164–5183, doi:10.3390/rs6065164.
- Cisewski, B., V. H. Strass, and H. Prandke (2005), Upper-ocean vertical mixing in the Antarctic Polar Front Zone, *Deep Sea Res., Part I*, *52*, 1087–1108, doi:10.1016/j.dsr2.2005.01.010.
- Cresswell, G. R. (1982), The coalescence of 2 east Australian current warm-core eddies, *Science*, *215*, 161–164, doi:10.1126/science.215.4529.161.
- Dong, C. M., J. C. McWilliams, Y. Liu, and D. K. Chen (2014), Global heat and salt transports by eddy movement, *Nat. Commun.*, *5*, 3294, doi:10.1038/ncomms4294.
- Ebuchi, E., and K. Hanawa (2001), Trajectory of mesoscale eddies in the Kuroshio recirculation region, *J. Oceanogr.*, *57*, 471–480, doi:10.1023/A:1021293822277.
- Elliott, B. A. (1982), Anticyclonic rings in the Gulf of Mexico, *J. Phys. Oceanogr.*, *12*, 1292–1309, doi:10.1175/1520-0485(1982)012<1292:ARITGO>2.0.CO;2.
- Gordon, A. L. (1985), Indian-Atlantic Transfer of thermocline water at the Agulhas retroflection, *Science*, *227*, 1030–1033, doi:10.1126/science.227.4690.1030.
- Hyun, K. H., and P. J. Hogan (2008), Topographic effects on the anticyclonic vortex evolution: A modeling study, *Cont. Shelf Res.*, *28*, 1246–1260, doi:10.1016/j.csr.2008.02.011.
- Ichikawa, K., S. Imawaki, and H. Ishii (1995), Comparison of surface velocities determined from altimeter and drifting buoy data, *J. Oceanogr.*, *51*, 729–740, doi:10.1007/BF02235462.
- Isoguchi, O., and H. Kawamura (2006), Oyashio seasonal intensification and its effect on subsurface temperature variation off the Sanriku coast, *J. Geophys. Res.*, *111*, C10006, doi:10.1029/2006JC003628.
- Ito, S., H. Sugisaki, A. Tsuda, O. Yamamura, and K. Okuda (2004), Contributions of the VENFISH program: Meso-zooplankton, Pacific saury (*Cololabis saira*) and walleye pollock (*Theragra chalcogramma*) in the northwestern Pacific, *Fish. Oceanogr.*, *13*, 1–9, doi:10.1111/j.1365-2419.2004.00309.x.
- Itoh, S., and T. Sugimoto (2001), Numerical experiments on the movement of a warm-core ring with the bottom slope of a western boundary, *J. Geophys. Res.*, *106*, 26,851–26,862, doi:10.1029/2001JC000789.
- Itoh, S., and I. Yasuda (2010a), Characteristics of mesoscale eddies in the Kuroshio-Oyashio extension region detected from the distribution of the sea surface height anomaly, *J. Phys. Oceanogr.*, *40*, 1018–1034, doi:10.1175/2009JPO4265.1.
- Itoh, S., and I. Yasuda (2010b), Water mass structure of warm and cold anticyclonic eddies in the western boundary region of the Subarctic North Pacific, *J. Phys. Oceanogr.*, *40*, 2624–2642, doi:10.1175/2010JPO4475.1.
- Itoh, S., I. Yasuda, T. Nakatsuka, J. Nishioka, and Y. N. Volkov (2010), Fine- and microstructure observations in the Urup Strait, Kuril Islands, during August 2006, *J. Geophys. Res.*, *115*, C08004, doi:10.1029/2009JC005629.
- Itoh, S., Y. Shimizu, S.-I. Ito, and I. Yasuda (2011a), Evolution and decay of a warm-core ring within the western subarctic gyre of the North Pacific, as observed by profiling floats, *J. Oceanogr.*, *67*, 281–293, doi:10.1007/s10872-011-0027-2.
- Itoh, S., I. Yasuda, M. Yagi, S. Osafune, H. Kaneko, J. Nishioka, T. Nakatsuka, and Y. N. Volkov (2011b), Strong vertical mixing in the Urup Strait, *Geophys. Res. Lett.*, *38*, L16607, doi:10.1029/2011GL048507.
- Itoh, S., I. Yasuda, H. Ueno, T. Suga, and S. Kakehi (2014a), Regeneration of a warm anticyclonic ring by cold water masses within the western subarctic gyre of the North Pacific, *J. Oceanogr.*, *70*, 211–223, doi:10.1007/s10872-014-0225-9.
- Itoh, S., Y. Tanaka, S. Osafune, I. Yasuda, M. Yagi, H. Kaneko, S. Konda, J. Nishioka, and Y. N. Volkov (2014b), Direct breaking of large-amplitude internal waves in the Urup Strait, *Prog. Oceanogr.*, *126*, 109–120, doi:10.1016/j.pocean.2014.04.014.
- Jayne, S. R., and J. Marotzke (2002), The oceanic eddy heat transport, *J. Phys. Oceanogr.*, *32*, 3328–3345, doi:10.1175/1520-0485(2002)032<3328:TOEHT>2.0.CO;2.
- Joyce, T., et al. (1984), Rapid evolution of a Gulf-Stream warm-core ring, *Nature*, *308*, 837–840, doi:10.1038/308837a0.
- Joyce, T. M., J. K. B. Bishop, and O. B. Brown (1992), Observations of offshore shelf-water transport induced by a warm-core ring, *Deep Sea Res., Part A*, *39*, S97–S113.
- Kaneko, H., I. Yasuda, K. Komatsu, and S. Itoh (2013), Observations of vertical turbulent nitrate flux across the Kuroshio, *Geophys. Res. Lett.*, *40*, 3123–3127, doi:10.1002/grl.50613.
- Kawai, H., and M. Sasaki (1962), On the hydrographic conditions accelerating the skipjack's northward movement across the Kuroshio front (in Japanese with English abstract), *Bull. Tohoku Reg. Fish. Res. Inst.*, *20*, 1–27.
- Kouketsu, S., H. Tomita, E. Oka, S. Hosoda, T. Kobayashi, and K. Sato (2012), The role of meso-scale eddies in mixed layer deepening and mode water formation in the western North Pacific, *J. Oceanogr.*, *68*, 63–77, doi:10.1007/s10872-011-0049-9.
- Nilsson, C. S., and G. R. Cresswell (1980), Formation and evolution of east Australian current warm core eddies, *Prog. Oceanogr.*, *9*, 133–184, doi:10.1016/0079-6611(80)90008-7.
- Nishikawa, H., I. Yasuda, and S. Itoh (2011), Impact of winter-to-spring environmental variability along the Kuroshio jet on the recruitment of Japanese sardine (*Sardinops melanostictus*), *Fish. Oceanogr.*, *20*, 570–582, doi:10.1111/j.1365-2419.2011.00603.x.
- Okunishi, T., et al. (2012), A modeling approach to evaluate growth and movement for recruitment success of Japanese sardine (*Sardinops melanostictus*) in the western Pacific, *Fish. Oceanogr.*, *21*, 44–57, doi:10.1111/j.1365-2419.2011.00608.x.
- Olson, D. B. (1986), Lateral exchange within Gulf Stream warm-core ring surface layers, *Deep Sea Res., Part A*, *33*, 1691–1704, doi:10.1016/0198-0149(86)90074-9.
- Olson, D. B. (1991), Rings in the ocean, *Annu. Rev. Earth Planet. Sci.*, *19*, 283–311, doi:10.1146/annurev.earth.19.1.283.
- Olson, D. B. (2001), Biophysical dynamics of western transition zones: A preliminary synthesis, *Fish. Oceanogr.*, *10*, 133–150, doi:10.1046/j.1365-2419.2001.00161.x.
- Qiu, B., and S. M. Chen (2005), Eddy-induced heat transport in the subtropical North Pacific from Argo, TMI, and altimetry measurements, *J. Phys. Oceanogr.*, *35*, 458–473, doi:10.1175/JPO2696.1.
- Richardson, P. L. (2007), Agulhas leakage into the Atlantic estimated with subsurface floats and surface drifters, *Deep Sea Res., Part I*, *54*, 1361–1389, doi:10.1016/j.dsr.2007.04.010.
- Roemmich, D., and J. Gilson (2001), Eddy transport of heat and thermocline waters in the North Pacific: A key to interannual/decadal climate variability?, *J. Phys. Oceanogr.*, *31*, 675–687, doi:10.1175/1520-0485(2001)031<0675:ETOHAT>2.0.CO;2.
- Saito, H., T. Suga, K. Hanawa, and N. Shikama (2011), The transition region mode water of the North Pacific and its rapid modification, *J. Phys. Oceanogr.*, *41*, 1639–1658, doi:10.1175/2011JPO4346.1.
- Shcherbina, A. Y., M. C. Gregg, M. H. Alford, and R. R. Harcourt (2010), Three-dimensional structure and temporal evolution of submesoscale thermohaline intrusions in the North Pacific Subtropical Frontal Zone, *J. Phys. Oceanogr.*, *40*, 1669–1689.
- Shiozaki, T., S.-I. Ito, K. Takahashi, H. Saito, T. Nagata, and K. Furuya (2014), Regional variability of factors controlling the onset timing and magnitude of spring algal blooms in the northwestern North Pacific, *J. Geophys. Res. Oceans*, *119*, 253–265, doi:10.1002/2013JC009187.

- Sugimoto, S., and K. Hanawa (2011), Roles of SST anomalies on the wintertime turbulent heat fluxes in the Kuroshio-Oyashio confluence region: Influences of warm eddies detached from the Kuroshio extension, *J. Clim.*, *24*, 6551–6561, doi:10.1175/2011JCLI4023.1.
- Sugimoto, T., and H. Tameishi (1992), Warm-core rings, streamers and their role on the fishing ground formation around Japan, *Deep Sea Res., Part A*, *39*, S183–S201.
- Sugimoto, T., Y. Kawasaki, and J. Li (1992), A description of the time-dependent hydrographic structure of the warm streamer around the Kuroshio Warm-core ring 86B, *Deep Sea Res., Part A*, *39*, S77–S96.
- Sutyryn, G. G., G. D. Rowe, L. M. Rothstein, and I. Ginis (2003), Baroclinic eddy interactions with continental slopes and shelves, *J. Phys. Oceanogr.*, *33*, 283–291, doi:10.1175/1520-0485(2003)033<0283:BEIWCS>2.0.CO;2.
- Talley, L. D., and J. Y. Yun (2001), The role of cabbeling and double diffusion in setting the density of the North Pacific intermediate water salinity minimum, *J. Phys. Oceanogr.*, *31*, 1538–1549, doi:10.1175/1520-0485(2001)031<1538:TROCAD>2.0.CO;2.
- Tomosada, A. (1986), Generation and decay of Kuroshio warm-core rings, *Deep Sea Res., Part A*, *33*, 1475–1486, doi:10.1016/0198-0149(86)90063-4.
- Ueno, H., and I. Yasuda (2005), Temperature inversions in the subarctic North Pacific, *J. Phys. Oceanogr.*, *35*, 2444–2456, doi:10.1175/JPO2829.1.
- Ueno, H., H. J. Freeland, W. R. Crawford, H. Onishi, E. Oka, K. Sato, and T. Suga (2009), Anticyclonic Eddies in the Alaskan Stream, *J. Phys. Oceanogr.*, *39*, 934–951, doi:10.1175/2008JPO3948.1.
- Ueno, H., I. Yasuda, S. Itoh, H. Onishi, Y. Hiroe, T. Suga, and E. Oka (2012), Modification of a Kenai eddy along the Alaskan Stream, *J. Geophys. Res.*, *117*, C08032, doi:10.1029/2011JC007506.
- Watanabe, Y. (2007), Latitudinal variation in the recruitment dynamics of small pelagic fishes in the western North Pacific, *J. Sea Res.*, *58*, 46–58, doi:10.1016/j.seares.2007.02.002.
- Yagi, M., and I. Yasuda (2012), Deep intense vertical mixing in the Bussol' Strait, *Geophys. Res. Lett.*, *39*, L01602, doi:10.1029/2011GL050349.
- Yasuda, I., and Y. Watanabe (1994), On the relationship between the Oyashio front and saury fishing grounds in the north-western Pacific: A forecasting method for fishing ground locations, *Fish. Oceanogr.*, *3*, 172–181, doi:10.1111/j.1365-2419.1994.tb00094.x.
- Yasuda, I., K. Okuda, and M. Hirai (1992), Evolution of a Kuroshio warm-core ring—Variability of the hydrographic structure, *Deep Sea Res., Part A*, *39*, S131–S161.
- Yasuda, I., K. Okuda, and Y. Shimizu (1996), Distribution and modification of north Pacific intermediate water in the Kuroshio-Oyashio inter-frontal zone, *J. Phys. Oceanogr.*, *26*, 448–465, doi:10.1175/1520-0485(1996)026<0448:DAMONP>2.0.CO;2.
- Yasuda, I., et al. (2000), Cold-core anticyclonic eddies south of the Bussol' Strait in the northwestern subarctic Pacific, *J. Phys. Oceanogr.*, *30*, 1137–1157, doi:10.1175/1520-0485(2000)030<1137:CCAESO>2.0.CO;2.